

# The effect of grain size on river delta process and morphology

Author: Rebecca Lee Caldwell

Persistent link: <http://hdl.handle.net/2345/bc-ir:104266>

This work is posted on [eScholarship@BC](#),  
Boston College University Libraries.

---

Boston College Electronic Thesis or Dissertation, 2013

Copyright is held by the author, with all rights reserved, unless otherwise noted.

Boston College

The Graduate School of Arts and Sciences

Department of Earth and Environmental Sciences

THE EFFECT OF GRAIN SIZE ON RIVER DELTA PROCESS AND MORPHOLOGY

a thesis

by

REBECCA LEE CALDWELL

submitted in partial fulfillment of the requirements

for the degree of

Master of Science

May, 2013



## **Abstract**

The effect of grain size on river delta process and morphology

Rebecca L. Caldwell

Advisor: Douglas Edmonds

Delta morphology is traditionally explained by differences in fluvial energy and wave and tidal energy. However, deltas influenced by similar ratios of river to marine energy can display strikingly different morphologies. Other variables, such as grain size of the sediment load delivered to the delta, influence delta morphology, but these models are largely qualitative leaving many questions unanswered. To better understand how grain size modifies deltaic processes and morphologies I conducted 33 numerical modeling experiments and quantified the effects produced by different grain sizes. In these 33 runs I change the median (0.01 – 1 mm), standard deviation (0.1 – 3  $\phi$ ), and skewness (-0.7 – 0.7) of the incoming grain-size distribution. The model setup includes a river carrying constant discharge entering a standing body of water devoid of tides, waves, and sea-level change. The results show that delta morphology undergoes a transition as median grain size and standard deviation increase while changing skewness has little effect. At small median grain size and standard deviation, deltas have elongate planform morphologies with sinuous shorelines characterized by shallow topset gradients ranging from  $1 \times 10^{-4}$  to  $3 \times 10^{-4}$ , and by 1 - 8 stable active channels. At large median grain size and standard deviation, deltas transition to semi-circular planform morphologies with smooth shorelines characterized by steeper topset gradients ranging from  $1 \times 10^{-3}$  to  $2 \times 10^{-3}$ , and by 14 - 16 mobile channels. The change in delta morphology can be morphodynamically linked to changes in grain size. As grain size increases delta

morphology transitions from elongate to semi-circular because the average topset gradient increases. For a given set of flow conditions, larger grain sizes require a steeper topset gradient to mobilize and transport. The average topset gradient reaches a dynamic equilibrium through time. This requires that, per unit length of seaward progradation, deltas with steeper gradients have higher vertical sedimentation rates. Higher sedimentation rates, in turn, perch the channel above the surrounding floodplain (so-called 'super-elevation'), resulting in unstable channels that frequently avulse and create periods of overbank flow. The overbank flow is more erosive because the steeper gradient causes higher shear stresses on the floodplain, which creates more channels. More channels reduce the average water and sediment discharge at a given channel mouth, which creates time scales for mouth bar formation in coarse-grained deltas that are longer than the avulsion time scale. This effectively suppresses the process of bifurcation around river mouth bars in coarse-grained deltas, which in turn creates semi-circular morphologies with smooth shorelines as channels avulse across the topset. On the other hand, the finest-grained (i.e. mud) deltas have low topset gradients and fewer channels. The high water and sediment discharge per channel, coupled with the slow settling velocity of mud, advects the sediment far from channel mouths, which in turn creates mouth bar growth and avulsion time scales that are longer than the delta life. This creates an elongate delta as stable channels prograde basinward. Deltas with intermediate grain sizes have nearly equal avulsion and bifurcation time scales, creating roughly semi-circular shapes but with significant shoreline roughness where mouth bars form.

## Table of Contents

Acknowledgements .....	ii
List of Figures .....	iii
List of Tables .....	v
1. Introduction .....	1
2. Background .....	4
3. Methods .....	9
3.1. Description of the Delft3D Model .....	9
3.2. Model Setup .....	12
3.3. Parameter Space .....	18
4. Results .....	22
4.1. Variation in Delta-Building Processes .....	26
4.2. Variation in Delta Channel Network and Planform Morphology .....	27
4.2.1. Description of Morphometric Parameters .....	28
4.2.2. Effect of Median Grain Size on Delta Channel Network and Planform Morphology .....	31
4.2.3. Effect of Cohesion on Delta Channel Network and Planform Morphology .....	38
5. Discussion .....	41
5.1. Does Median Grain Size Control Topset Gradient? .....	41
5.2. How Does Median Grain Size Control the Number of Channel Mouths? .....	44
5.3. How Does Cohesion Control the Number of Channel Mouths? .....	49
5.4. Process-Based Model for Grain Size Effects on Delta Channel Network Morphology and Planform Morphology .....	51
5.5. Influence of Catchment Characteristics on Delta Morphology .....	53
6. Conclusion .....	55
Notation .....	57
REFERENCES .....	59

## **Acknowledgements**

This research was funded by the National Science Foundation (OCE-1061380) awarded to Douglas Edmonds.

Thank you to my advisor, Douglas Edmonds, for putting up with me for as long as you have and somehow agreeing to continue through a second degree. Your guidance has helped me grow into a more capable researcher and your encouragement has supported me through the long hours. Let's keep it up over the next few (fingers crossed) years.

I would also like to thank my professors at Boston College for teaching me the ways of the geologic world. Special thanks to my committee members, Gail Kineke and John Ebel, for extending that teaching to my thesis work.

Similarly, I want to thank my fellow graduate students. You all have taught me just as much as my professors have, and I will (somehow) miss working through seemingly impossible problem sets late into the night together.

Finally, thanks to my Mom. You are an inspiration and source of never-ending support. I don't know how I could have done this without you.

## List of Figures

Figure 1. Deltas with similar ratios of marine to fluvial energy ( $M_p:R_p$ ) have different morphologies from (A) elongate to (B) semi-circular to (C) braided. Data from (A and C) <i>Syvitski and Saito</i> [2007] and (B) <i>Edmonds</i> [unpublished].	2
Figure 2. Delta morphology is related to grain size in addition to river, wave, and tidal energy (modified from <i>Orton and Reading</i> , 1993).	5
Figure 3. Numerical model setup in planview. Modeling domain consists of grid cells that are 25 x 25 meters. Colors represent initial bathymetry. Black arrow indicates direction of incoming flow. Thick black border lines indicate open boundaries of constant water surface elevation at 0 m.	13
Figure 4. Example grain-size distributions showing (A) discretization of a continuous grain-size distribution into seven sediment fractions represented as a histogram (example shown for $D_{50} = 0.1$ mm, $\sigma = 2 \phi$ ), (B) the ranges in median grain sizes (examples shown for $\sigma = 1 \phi$ ), and (C) the ranges in standard deviations (examples shown for $D_{50} = 0.1$ mm). The location of Delft3D's cohesive grain size threshold is included for reference within phi space.	19
Figure 5. Delft3D model results that show different delta morphologies created from different grain-size distributions. Deltas are pictured when the same volume of sediment has entered the system. Median grain diameters (y-axis) are expressed in phi values with size in mm shown in brackets. Standard deviations are expressed in phi values. Note that both x- and y-axis intervals vary. For all runs skewness = 0.	23
Figure 6. Model deltas under varying skewness of the grain-size distribution (x-axis) and median grain size (y-axis). The deltas in the middle column (skewness = 0) are the same results presented in Figure 5. Little to no morphological variation exists along the x-axis. Note that the y-axis intervals vary. For all runs $\sigma = 1 \phi$ .	24
Figure 7. Relationship between median grain size and key morphometric parameters: (a) topset gradient (grouped by standard deviation); (b) topset gradient (grouped by percent cohesion); and (c) average number of channel mouths (grouped by standard deviation).	25
Figure 8. Evolution of fine (a-c), intermediate (d-f), and coarse (g-i) grained deltas. (b-c): brackets highlight northwest channel elongation. (e-f): arrows show shoreline deviations $\sim 4-6$ channel widths in length. The x-axis represents relative delta growth, where $t$ is time and $T$ is total time. $T$ is calculated when a predetermined volume of sediment has entered the system. Runs shown here have $\sigma = 1 \phi$ and skewness = 0.	27
Figure 9. Cartoons depicting how (a) shoreline rugosity (Run ID = B1c1, rugosity value $\approx 1.6$ ) and (b) bulk delta shape (Run ID = C1m1, bulk shape value $\approx 0.9$ ) are measured. See text for description of calculations.	30
Figure 10. Measured topset gradients (a) contoured in the $D_{50}$ vs. $\sigma$ parameter space, and (b) with the contours from (a) superimposed on the images of model deltas.	34

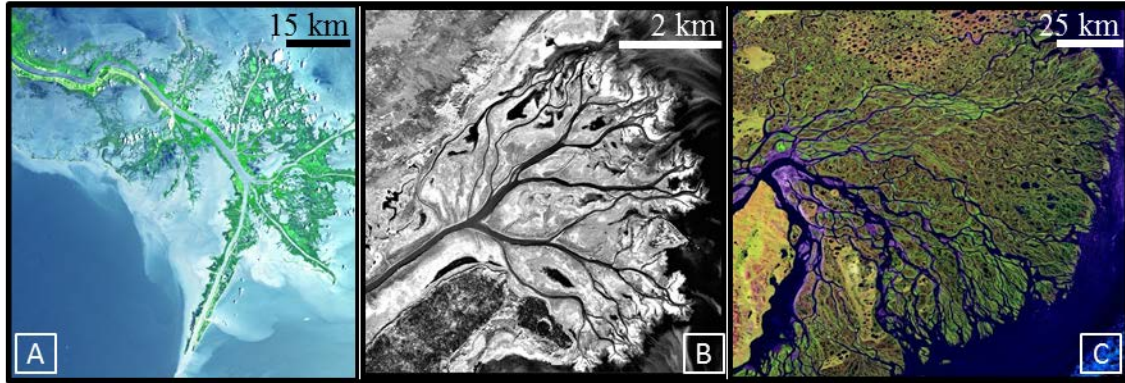
Figure 11. Measured average number of channel mouths (a) contoured in the $D_{50}$ vs. $\sigma$ parameter space, and (b) with the contours from (a) superimposed on the images of model deltas.....	35
Figure 12. Distribution of measured shoreline rugosity, calculated as shoreline sinuosity (actual shoreline length / smoothed shoreline shape), (a) contoured in the $D_{50}$ vs. $\sigma$ parameter space, and (b) with the contours from (a) superimposed on the images of model deltas. ....	36
Figure 13. Distribution of measured bulk delta shape, calculated as $X = W_d / 2L_d$ , (a) contoured in the $D_{50}$ vs. $\sigma$ parameter space, and (b) with the contours from (a) superimposed on the images of model deltas. ....	37
Figure 14. Percent cohesive sediment that makes up the incoming sediment load (a) contoured in the $D_{50}$ vs. $\sigma$ parameter space, and (b) with the contours from (a) superimposed on the images of model deltas. ....	39
Figure 15. Relationship between percent cohesive sediment and (A) topset gradient, and (B) average number of channel mouths. Colors denote median grain size....	40
Figure 16. Predicted topset gradients ( $S$ in equation 10) vs. measured topset gradients. Black line denotes perfect agreement. ....	42
Figure 17. Measured topset gradient throughout delta growth shows topset gradient reaches a dynamic equilibrium after $t/T$ of $\sim 0.1$ for C1h1 and C1o1, and after $t/T$ of $\sim 0.3$ for C1a1. Representative examples shown for fine (C1a1, $D_{50} = 0.01$ mm), intermediate (C1h1, $D_{50} = 0.25$ mm), and coarse (C1o1, $D_{50} = 1$ mm) grained deltas. The x-axis represents relative delta growth, where $t$ is time and $T$ is total time. Runs shown here have $\sigma = 2 \phi$ .....	43
Figure 18. Ratio of channelized grid cells that are still ‘active’ after channel initiation ( $R_{ch}$ ) (solid lines) and decay curves fit to each abandonment rate (dashed lines). Examples shown here are for channels that formed at $t/T = 0.6$ , where $t$ is time and $T$ is total time. Thus, $t/T = 0.6$ corresponds to $i = 0$ in this case. Complete abandonment is defined as the abandonment of 90% of the initially active channel cells, shown here as a dotted line. Examples shown for fine (C1a1, $D_{50} = 0.01$ mm), intermediate (C1h1, $D_{50} = 0.25$ mm), and coarse (C1o1, $D_{50} = 1$ mm) grained deltas. Runs shown here have $\sigma = 2 \phi$ . ....	46
Figure 19. Measured $Tch$ values and theoretical $T_A$ values plotted against median grain size ( $D_{50}$ ). $T_A$ is a theoretical avulsion frequency based on average channel depth and aggradation rates, and $Tch$ is measured channel-switching frequency. Vertical bars on $Tch$ represent measured standard deviation. See text for description of calculations.....	48

## List of Tables

Table 1. Model Parameters .....	14
Table 2. Model Run IDs and Sediment Parameters .....	15
Table 3. Sensitivity Runs Testing User-Defined Model Parameters .....	17

## 1. Introduction

The morphology of deltaic lobes is thought to be a function of the ratios of fluvial, wave, and tidal energies [*Galloway, 1975*]. While attractive in its simplicity, these variables do not explain the breadth of delta morphology seen the world over. For example, the Mississippi, Mossy, and Lena deltas have similar ratios of fluvial to marine (wave and tidal) energy, which suggests they should look alike, yet their morphologies range from an elongate shape with few distributary channels, to a rugose semi-circle with a bifurcated channel network, to a smooth semi-circle with a braided channel pattern (Figure 1). This indicates that delta morphology may be controlled by additional variables. Interestingly, the sediment loads contributing to the growth of these three deltas have median grain sizes that range from silt to sand [*Syvitski and Saito, 2007*; *Edmonds, unpublished*]. Delta morphology has been linked to grain size of the incoming sediment load, but this effect has never been quantified or tested because separating cause and effect in natural deltas is difficult. Here I suggest how grain size may exert a control on delta morphology and show later, using numerical modeling of delta formation, how the variation in delta channel network and planform morphology can be explained in a grain size framework.



Mississippi Delta	Mossy Delta	Lena Delta
$D_{50} = 0.014 \text{ mm}$	$D_{50} = 0.125 \text{ mm}$	$D_{50} = 0.3-0.6 \text{ mm}$
$M_p:R_p = 0.1$	$M_p:R_p = \text{minimal}$	$M_p:R_p = 0.2$

**Figure 1.** Deltas with similar ratios of marine to fluvial energy ( $M_p:R_p$ ) have different morphologies from (A) elongate to (B) semi-circular to (C) braided. Data from (A and C) *Syvitski and Saito* [2007] and (B) *Edmonds* [unpublished].

The idea that grain size controls delta morphology is not new [e.g. *McPherson et al.*, 1987; *Orton and Reading*, 1993]; however, the previous research is largely qualitative. For example, this early work demonstrated that deltas constructed from larger median grain sizes tend to be semi-circular, whereas fine-grained deltas exhibit more irregular shapes in planview [*McPherson et al.*, 1987; *Orton and Reading*, 1993]. But, it is not obvious how these morphologies arise and if or how they are set by grain size.

The purpose of this study is to provide a process-based understanding of how grain size influences deltaic processes, and thus morphology. By numerically modeling delta growth under varying grain-size distributions, I aim to elucidate how grain size controls delta-building processes and resulting morphology. My results show that as both median grain size and standard deviation of the grain-size distribution increase, a morphological transition from elongate deltas with a few channels to semi-circular deltas

with many, mobile channels occurs. The change in delta morphology can be morphodynamically linked to changes in grain size. Results show that grain size can control the delta topset gradient, which reaches a dynamic equilibrium through time. Vertical sedimentation rates adjust to maintain topset gradients, which affects channel avulsion frequency and overbank flow, and ultimately sets the number of channel mouths along the delta shoreline. The number of channel mouths and advection lengths of varying grain sizes set the depositional pattern along the shoreline, which translates into shoreline rugosity and delta shape patterns. A process-based model for effect of grain size is presented, describing how changes in grain size shift deltas into different process-based regimes, where a dominant growth process is expressed through the resulting morphology.

## 2. Background

The factors that influence delta morphology can be grouped into those that originate upstream or downstream from the delta. Upstream factors control delta morphology via the fluvial system, such as river discharge [e.g. *Hooke and Rohrer*, 1979; *Edmonds et al.*, 2010], feeder system geometry and pattern [e.g. *Postma*, 1990; *Geleynse et al.*, 2010], and rates and properties of sediment input [e.g. *Postma*, 1990; *Orton and Reading*, 1993]. Downstream factors control delta morphology via marine processes such as buoyancy, waves [e.g. *Bhattacharya and Giosan*, 2003; *Jerolmack and Swenson*, 2007], tides [e.g. *Dalrymple and Choi*, 2007], and sea-level variations [*Jerolmack*, 2009].

*Galloway* [1975] (bottom right of Figure 2) suggested that the balance between upstream fluvial energy and downstream wave and tidal energy controls delta morphology. He claimed that fluvial energy generated by river discharge promotes basinward channel progradation, resulting in elongate deltas such as the Mississippi. Downstream marine forces generated by waves and tides work to redistribute sediment delivered to the delta apex along the adjacent shoreline. *Galloway's* classification was semi-quantitative and only recently have studies started to show how waves and tides affect delta processes. In general, wave energy creates broad, often asymmetric, smooth shorelines by setting up along-shore currents that redistribute sediment lateral to the shoreline and suppress mouth bar formation [*Jerolmack and Swenson*, 2007; *Ashton and Giosan*, 2011; *Nardin and Fagherazzi*, 2012]. Additionally, wave energy has been shown to create shoreline perturbations [*Ashton and Giosan*, 2011] and influence mouth bar formation patterns [*Nardin and Fagherazzi*, 2012] due to varying degrees of wave amplitude and angle to the shoreline. Tides cause the remobilization of sediment,

eroding mouth bars and maintaining abandoned distributary channels, which results in delta morphologies characterized by dendritic channel networks with a large number of distributaries that widen basinward [Dalrymple and Choi, 2007; Fagherazzi and Overeem, 2007; Fagherazzi, 2008].

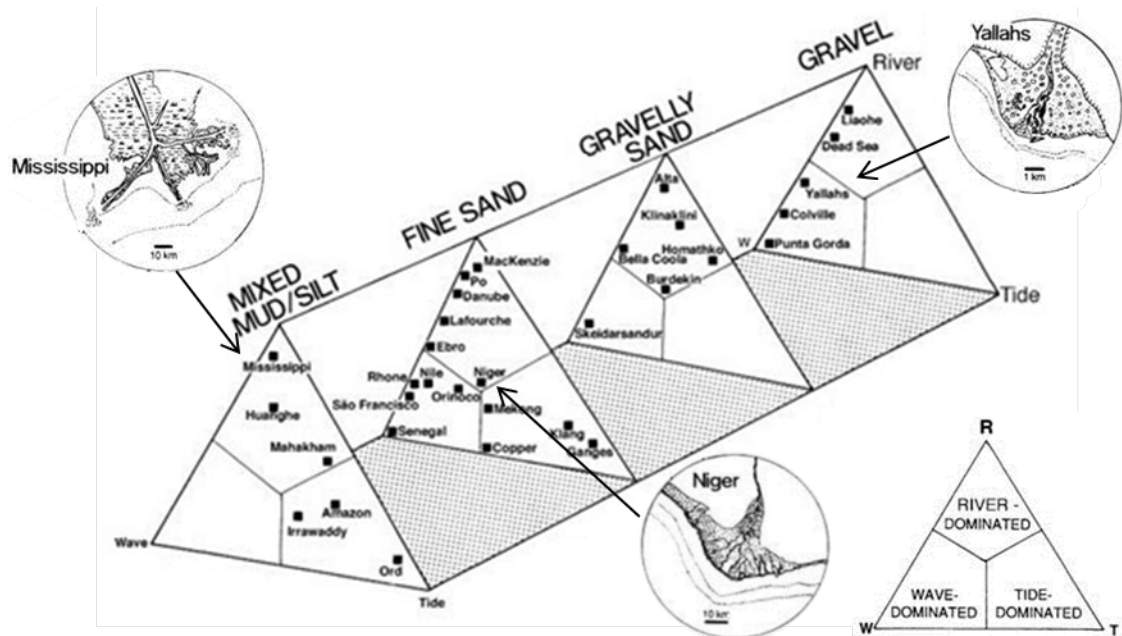


**Figure 2.** Delta morphology is related to grain size in addition to river, wave, and tidal energy (modified from *Orton and Reading, 1993*).

As pointed out previously (Figure 1) the classification by *Galloway [1975]* is incomplete and does not explain the full variability in delta morphology. Among the first to recognize this, *Orton and Reading [1993]* added a fourth axis to *Galloway's* classification diagram that accounts for grain size (Figure 2). As median grain size increases from silt to gravel, the resulting planform delta morphology transitions from elongate to braided and semi-circular [*McPherson et al., 1987; Orton and Reading, 1993*]. Fine-grained, elongate deltas are characterized by large, stable distributaries with low gradients and straight to sinuous patterns, and a delta plain area that is largely

subaqueous. In contrast, coarse-grained deltas have a larger number of small, ephemeral distributaries with a higher gradient and a braided pattern, and a delta plain that is largely (>70%) subaerial [*Orton and Reading, 1993*]. As catchment size and relief are largely responsible for the grain size delivered to the delta, this suggests a possible predictive link between the morphology of the delta and its catchment. These studies have identified median grain size as an important factor in determining delta morphology, but how changes in grain size modify processes and produce different morphologies is unknown.

The next logical step is to explore, from a process-based perspective, why and how the link between delta morphology and grain size exists. Recent progress has been made through the use of physical [*Hoyal and Sheets, 2009; Martin et al., 2009*] and numerical [*Edmonds and Slingerland, 2010; Geleynse et al., 2011*] experiments of delta formation. *Edmonds and Slingerland* [2010] investigated how sediment cohesion controls delta morphodynamics by changing ratios of cohesive to non-cohesive sediment entering the system and values of critical shear stress for erosion of the cohesive sediment. More cohesive sediment builds stronger levees, allowing channels to prograde basinward and produce rugose shorelines. In contrast, less cohesive conditions build weaker levees that distribute sediment across the entire delta plain, producing semi-circular deltas with smoother shorelines. *Geleynse et al.* [2011] used numerical modeling to show that subsurface sediment composition controls delta morphology in a similar way. Higher ratios of fine sediment present in the initial basin subsurface produce elongate features with incisive distributaries independent of grain-size ratios entering the

system. Furthermore, this effect is evident in the presence of both waves and tides, suggesting sediment properties may exert a stronger control than previously thought.

The preceding discussion demonstrates that our understanding of how sediment properties affect delta morphology remains incomplete. Predictions based on extensive observations of modern deltas and a few quantitative studies suggest that delta morphology is strongly dependent on sediment properties. Specifically, changes in grain size [e.g. *Orton and Reading, 1993*] and cohesive to non-cohesive sediment ratios [*Edmonds and Slingerland, 2010; Geleynse et al., 2011*] produce morphological transitions from elongate to semi-circular deltas. Exactly how this morphological transition evolves and what aspects of the grain-size distribution control it remain unknown.

I hypothesize that grain size controls delta morphology in two key ways. First, the transport slope of the delta system is set by a representative size of the grain-size distribution. Steeper transport slopes required for coarser grains lead to higher aggradation rates which affect channel stability and the resulting channel network morphology. Second, the median grain size and the shape of the grain-size distribution control the percentage of cohesive sediment entering the domain. Previous results have shown that cohesive sediment does exert a significant control on delta morphology [*Edmonds and Slingerland, 2010; Geleynse et al., 2011*]. I expand the parameter space to include both completely cohesive deltas and non-cohesive deltas. I expect the control by cohesive sediment to be present in the resulting channel network and shoreline rugosity.

Given the great importance of deltaic systems as modern resources [*Syvitski and Saito, 2007*] and as stratigraphic links to understanding past environments, there is a

pressing need for understanding how the morphologies of deltaic systems arise. To this end, my approach is to numerically model delta growth under varying grain size to provide a process-based link between delta morphology and grain size, which is something field studies [e.g. *Orton and Reading, 1993*] have struggled to do. The important objectives of this study are to quantify (1) the extent to which changes in the median, standard deviation, and skewness of the grain-size distribution modify delta-building processes, and (2) how these changes produce variations in channel network morphology and delta planform morphology.

This study differs from similar recent studies [*Edmonds and Slingerland, 2010; Geleynse et al., 2011*] in a few key ways. The explicit aim here is to explore how the grain-size distribution controls delta process and morphology. I focus on grain-size distribution because that is a variable that is easily constrained and measured in the field. The previous studies focused primarily on the effects of cohesive sediments and the grain-size distributions in the models were represented by only one or two grain sizes. Furthermore, the past studies did not consider the full range of sediment conditions, but I systematically consider the variation from coarse-grained bedload dominated deltas to fine-grained suspended load dominated ones in one study.

### 3. Methods

#### 3.1. Description of the Delft3D Model

I model deltaic processes and formation using Delft3D, which is a physics-based morphodynamic model that simulates flow and sediment transport. The program has been validated for various hydrodynamic and sediment transport studies [*Lesser et al.*, 2004; *Edmonds and Slingerland*, 2007; *van Maren*, 2007; *Edmonds and Slingerland*, 2008; *Hu et al.*, 2009; *van Maren et al.*, 2009; *Edmonds and Slingerland*, 2010] including models of delta growth [*Marciano et al.*, 2005; *Dastgheib et al.*, 2008; *Edmonds and Slingerland*, 2010; *Geleynse et al.*, 2010; *Geleynse et al.*, 2011]. Flow is computed using the depth-integrated Reynolds-averaged Navier-Stokes equations for incompressible, free surface flow. Hydrodynamic results are then used to compute suspended and bedload transport using the transport formulation from *Van Rijn* [1993], and the bed elevation is subsequently updated according to the location and magnitude of fluxes in sediment transport. This computation loop follows a prescribed time stepping procedure until run time is complete, which I define as the time at which an equal amount of sediment has entered the system and the delta system has reached a dynamic steady state. Dynamic steady state occurs when morphometric variables, such as topset gradient and channel number, fluctuate around a mean value that does not vary with time. The remaining discussion of Delft3D will focus on the mathematical treatment of sediment transport for cohesive and non-cohesive grains. For further description of hydrodynamic calculations see *Deltares* [2011].

Delft3D models each grain size as a separate fraction of the total sediment load. Sediment transport calculations are computed separately for each grain size fraction and

applied to the total sediment load according to each fraction's weight percent and availability in the topmost bed layer. Delft3D records a layered bed stratigraphy that keeps track of sediment deposition. The topmost bed layer is updated according to local erosional and depositional fluxes of each grain size fraction, and when a threshold layer thickness is reached the layer is recorded in the subsurface and a new one started. Only sediments in the topmost layer are available for erosion.

Cohesive and non-cohesive sediment transport, erosion, and deposition are handled separately in Delft3D. Any sediment fraction  $\leq 64 \mu\text{m}$  in diameter is considered cohesive sediment in the model, whereas those  $> 64 \mu\text{m}$  in diameter are non-cohesive. Cohesive sediment is only transported in suspension, whereas non-cohesive sediment is transported as both suspended load and bedload.

Transport of cohesive and non-cohesive suspended sediment is computed by solving the depth-averaged version of the 3D advection-diffusion equation:

$$\begin{aligned} \frac{\partial c^i}{\partial t} + \frac{\partial uc^i}{\partial x} + \frac{\partial vc^i}{\partial y} + \frac{\partial (w - w_s^i)c^i}{\partial z} \\ = \frac{\partial}{\partial x} \left( \varepsilon^i_{s,x} \frac{\partial c^i}{\partial x} \right) + \frac{\partial}{\partial y} \left( \varepsilon^i_{s,y} \frac{\partial c^i}{\partial y} \right) + \frac{\partial}{\partial z} \left( \varepsilon^i_{s,z} \frac{\partial c^i}{\partial z} \right) \end{aligned} \quad (1)$$

where  $c^i$  is the mass concentration of the  $i$ th sediment fraction ( $\text{kg}/\text{m}^3$ ) assuming a standard Rouse profile concentration gradient,  $u$ ,  $v$ , and  $w$  are the  $x$ -,  $y$ -, and  $z$ -directed fluid velocities ( $\text{m}/\text{s}$ ),  $w_s^i$  is the settling velocity of the  $i$ th sediment fraction ( $\text{m}/\text{s}$ ), and  $\varepsilon^i_{s,x}$ ,  $\varepsilon^i_{s,y}$ , and  $\varepsilon^i_{s,z}$  are directional eddy diffusivities of the  $i$ th sediment fraction ( $\text{m}^2/\text{s}$ ). Settling velocities of cohesive sediment fractions are set according to Stokes' law, and the effects of cohesive sediment flocculation are ignored. Non-cohesive sediment settling

velocities are calculated according to *Van Rijn* [1993] depending on the user-defined grain diameter, such that:

$$w_s^i = \begin{cases} \frac{(s-1)gD_{50}^i{}^2}{18\nu}, & 65 \mu\text{m} < D_{50}^i < 100 \mu\text{m} \\ \frac{10\nu}{D_{50}^i} \left( \sqrt{1 + \frac{0.01(s-1)gD_{50}^i{}^3}{\nu^2}} - 1 \right), & 100 \mu\text{m} < D_{50}^i < 1000 \mu\text{m} \\ 1.1\sqrt{(s-1)gD_{50}^i}, & 1000 \mu\text{m} < D_{50}^i \end{cases} \quad (2)$$

where  $s$  is the relative density ( $\rho_s/\rho_w$ ),  $\rho_s$  is the specific density of sediment ( $\text{kg/m}^3$ ),  $\rho_w$  is the specific density of water ( $\text{kg/m}^3$ ),  $g$  is acceleration due to gravity ( $9.8 \text{ m/s}^2$ ),  $D_{50}^i$  is the median grain diameter of the  $i$ th grain size fraction (m), and  $\nu$  is the kinematic viscosity coefficient of water ( $\text{m}^2/\text{s}$ ).

The transport of non-cohesive bedload is calculated by the method described by *Van Rijn* [1993]:

$$S_b = 0.006\rho_s w_s^i D_{50}^i \left( \frac{u(u - u_{cr})^{1.4}}{\left( (s-1)gD_{50}^i \right)^{1.2}} \right) \quad (3)$$

where  $u$  is depth-averaged velocity (m/s), and  $u_{cr}$  is the critical depth-averaged velocity (m/s) for initiation of motion based on a parameterization of the Shields curve. The direction of bedload transport is determined by local flow conditions and is adjusted for bed-slope effects [*Bagnold*, 1966; *Ikeda*, 1982]. While suspended load transport entering the upstream open boundary is prescribed by the user, the bedload transport is determined by local hydrodynamic conditions. Thus, time-averaged bedload sediment fluxes vary minimally between simulations.

Erosion and deposition of cohesive sediment is calculated according to the Partheniades-Krone formulations [Partheniades, 1965], which require a user-defined critical shear stress for erosion ( $\tau_{ce(C)}$ ) and deposition ( $\tau_{cd(C)}$ ). Exchange of non-cohesive suspended sediment with the bed is calculated as an erosive flux due to upward diffusion and depositional flux due to sediment settling. These fluxes are then applied as source and sink terms and the bed level is updated accordingly.

### 3.2. Model Setup

The experimental setup is based on the runs in *Edmonds and Slingerland* [2010]. An initial grid of 300 x 225 computation cells, each 25 x 25 m, creates a 7500 x 5625 m basin with a bed slope of 0.000375 to the north (Figure 3). Open boundaries of constant water surface elevation at 0 m border the north, east, and west boundaries of the grid (thick black lines in Figure 3), and there is an absence of waves, tides, and buoyancy forces within the basin. In the subsurface there is initially 10 m of erodible sediment that is homogeneously mixed and in the same proportions to the incoming grain-size distribution for each respective run. An initial bed roughness with amplitudes of a few centimeters is imposed on the basin floor, and a spatially constant Chézy value ( $C$ ) of 45 is used for hydrodynamic roughness, calculated as  $C = (8g/f)^{1/2}$  where  $g$  is acceleration due to gravity and  $f$  is the Darcy-Weisbach friction factor. Flow enters from the south through an initial channel 250 m wide and 2.5 m deep. The channel is 500 m long and is cut through an erodible beach 5.5 m in elevation above water level. The high elevation does not allow any water flow over the initial beach, thereby confining all water to the channel. The channel is allowed to change width and depth in response to different conditions. I specify a temporally constant water discharge of  $Q = 1000 \text{ m}^3/\text{s}$  to enter the

basin and to carry an equilibrium concentration of non-cohesive bedload and user-defined concentrations of cohesive sediment and non-cohesive suspended load. Each model is run for 16.5 days using a morphological bed updating factor of 175, resulting in ~8 years of morphological evolution in the model. This effectively models 8 years of bankfull flow conditions, and if flood intermittency (e.g., say a river is in bankfull condition on average 10 days a year) is accounted for, these results represent ~292 years of change in delta morphology. A sub-grid horizontal large eddy simulation calculates horizontal eddy viscosity and diffusivity, which are added to the constant background values set to  $0.0001 \text{ m}^2/\text{s}$ . Refer to (Table 1) for a list of all user-defined model parameters used in this study.

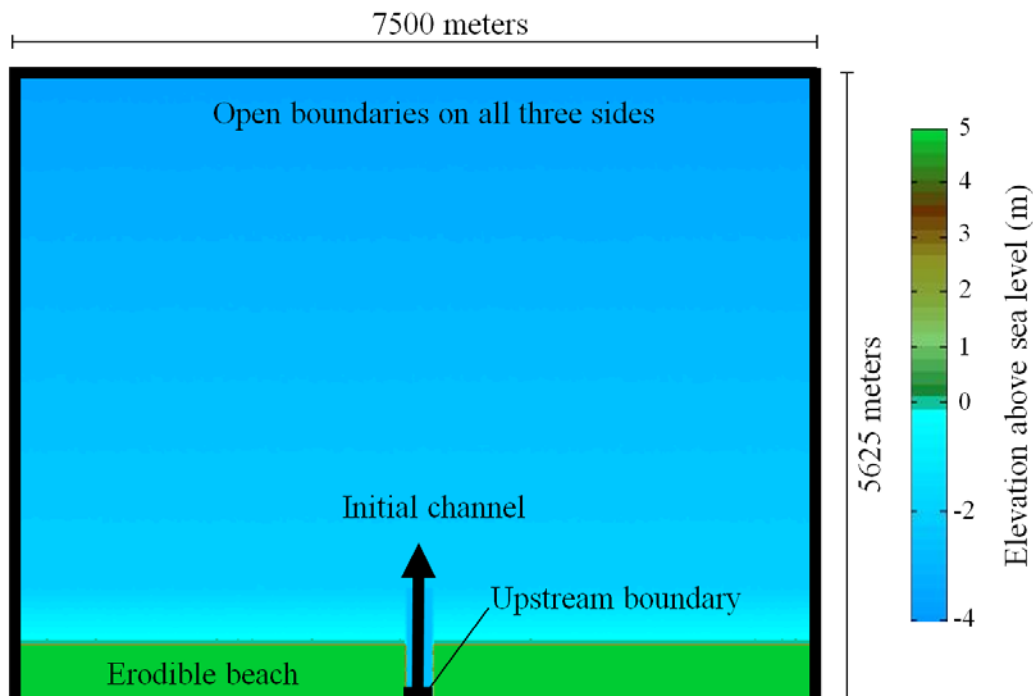


**Figure 3.** Numerical model setup in planview. Modeling domain consists of grid cells that are 25 x 25 meters. Colors represent initial bathymetry. Black arrow indicates direction of incoming flow. Thick black border lines indicate open boundaries of constant water surface elevation at 0 m.

**Table 1.** Model Parameters

User-Defined Model Parameter	Value	Units
Grid size	300 x 225	cells
Cell size	25 x 25	m
Initial basin bed slope	0.000375	-
Initial channel dimensions (width x depth)	250 x 2.5	m
Upstream open boundary: incoming water discharge	1000	m <sup>3</sup> /s
Downstream open boundary: constant water surface elevation	0	m
Initial sediment layer thickness at bed	10	m
Number of sediment fractions	7	-
Cohesive sediment critical shear stress for erosion ( $\tau_{ce(C)}$ )	1	N/m <sup>2</sup>
Cohesive sediment critical shear stress for deposition ( $\tau_{cd(C)}$ )	1000	N/m <sup>2</sup>
Time step	0.2	min.
Chézy value	45	m <sup>1/2</sup> /s
Background horizontal eddy viscosity and diffusivity (added to sub-grid horizontal large eddy simulation)	0.0001	m <sup>2</sup> /s
Morphological scale factor	175	-
Spin-up interval before morphological updating begins	720	min.
Factor for erosion of adjacent dry cells	0.33	-
Bed stratigraphy layer thickness	0.1	m

Sediment enters the system through the upstream open boundary of the initial channel (Figure 3). The suspended transport rate for cohesive and non-cohesive sediment totals 0.1 kg/m<sup>3</sup> (expressed as a volumetric flux it is  $Q_s = 0.0377$  m<sup>3</sup>/s) and is held constant throughout each run. This number was chosen because it is representative for deltas of the world [Sylvitski and Saito, 2007]. As previously described, bedload transport rates ( $Q_b$ ) entering the system are a product of time-varying hydrodynamic conditions at the upstream open boundary. Subsequently, time-averaged total sediment fluxes ( $\overline{Q}_t$ ) vary among runs (Table 2).

**Table 2.** Model Run IDs and Sediment Parameters<sup>a</sup>

Run ID	$D_{50}$ (mm)	Std ( $\phi$ )	Skewness <sup>b</sup>	% Cohesive	$\overline{Q}_t$ ( $\text{m}^3\text{s}^{-1}$ )
A1a1	0.01	0.1	0	100	0.0377
B2a1	0.01	1	0.7	100	0.0377
B1a1	0.01	1	0	98.13	0.0378
B3a1	0.01	1	-0.7	97.36	0.0378
C1a1	0.01	2	0	96.29	0.0378
D1a1	0.01	3	0	71.77	0.0386
A1c1	0.05	0.1	0	100	0.0377
B2c1	0.05	1	0.7	78.03	0.0379
B1c1	0.05	1	0	73.35	0.0380
B3c1	0.05	1	-0.7	53.51	0.0379
C1c1	0.05	2	0	72.85	0.0382
D1c1	0.05	3	0	71.07	0.0388
A1e1	0.1	0.1	0	0	0.0491
B2e1	0.1	1	0.7	44.30	0.0388
B1e1	0.1	1	0	26.17	0.0402
B3e1	0.1	1	-0.7	20.26	0.0415
C1e1	0.1	2	0	24.36	0.0414
D1e1	0.1	3	0	23.37	0.0431
A1h1	0.25	0.1	0	0	0.0520
B2h1	0.25	1	0.7	7.91	0.0455
B1h1	0.25	1	0	3.28	0.0481
B3h1	0.25	1	-0.7	0	0.0520
C1h1	0.25	2	0	24.52	0.0412
D1h1	0.25	3	0	19.92	0.0556
A1m1	0.5	0.1	0	0	0.0518
B2m1	0.5	1	0.7	1.64	0.0499
B1m1	0.5	1	0	0.04	0.0510
B3m1	0.5	1	-0.7	0	0.0556
C1m1	0.5	2	0	2.94	0.0512
D1m1	0.5	3	0	22.94	0.0420
A1o1	1	0.1	0	0	0.0500
B1o1	1	1	0	0	0.0495
C1o1	1	2	0	1.66	0.0508

<sup>a</sup>Variations in grain-size distributions that create unreasonable distributions (i.e. unrealistically large grain sizes) were not included in model runs.

<sup>b</sup>Variations in skewness performed only for subset of runs with  $\sigma = 1 \phi$ .

For each model run the incoming sediment flux consists of seven different grain sizes, represented as sediment fractions. A sediment fraction is a user-controlled parameter used to discretize the theoretically continuous grain-size distribution (Figure 4a). Each sediment fraction is assigned a grain size diameter and frequency, or representative fraction of the total incoming sediment flux. It follows that using more sediment fractions creates a more highly resolved grain-size distribution. Sensitivity tests varying the number of sediment fractions showed that a grain-size distribution discretized by seven sediment fractions results in the same overall delta shape, shoreline characteristics, and channel network as a higher resolution grain-size distribution of 14 fractions.

Delft3D requires the user to define values for critical shear stress for erosion ( $\tau_{ce(C)}$ ) and deposition ( $\tau_{cd(C)}$ ) of the cohesive sediment fractions. I set  $\tau_{ce(C)} = 1 \text{ N/m}^2$ , which represents a mud of intermediate cohesion [Black *et al.*, 2002]. There is considerable debate concerning the value of  $\tau_{cd(C)}$  in natural sediments [Black *et al.*, 2002]. By setting  $\tau_{cd(C)} = 1000 \text{ N/m}^2$  mud is continuously deposited, and the flow field adjusts until the erosional flux and depositional flux are equal. This avoids the issue of mutually exclusive erosion and deposition of cohesive sediment, which occurs when  $\tau_{cd(C)} < \tau_{ce(C)}$ . I avoid mutually exclusive erosion and deposition in the current runs because if  $\tau_{cd(C)} < \tau_{ce(C)}$  then cells would erode until the shear stress is less than  $\tau_{ce(C)}$ , which would result in an equilibrium form highly dependent on the chosen  $\tau_{ce(C)}$  value. Additionally, the effects of flocculation on cohesive sediment settling velocity are ignored.

I conducted a suite of test runs to assess the sensitivity of the results to user-defined model parameters (Table 3). Changing these parameters indeed created different deltas, but the deltas were only different in the details. There was little variation in delta shape, shoreline characteristics, and number of channels, which are the morphometric parameters of interest for this study.

**Table 3.** Sensitivity Runs Testing User-Defined Model Parameters<sup>a</sup>

<b>User-Defined Model Parameter</b>	<b>Values Tested</b>	<b>[<math>D_{50}(\text{mm})/\text{Std}(\phi)</math>]</b>
Grid resolution <sup>b</sup>	25 x 25 meters, 10 x 10 meters	[0.1/1], [1/0.1]
Number of sediment fractions	1, 3, 5, 7, 14	[0.05/1]
Time step	0.05, 0.1, 0.2, 1 (min.)	[0.1/1]
Morphological Scale Factor	50, 100, 175, 300	[0.1/1]
Bedload transport formulation <sup>b</sup>	van Rijn [1993], Meyer-Peter-Muller [1948], Engelund-Hansen [1967]	[0.01/1], [0.5/1]
Roughness formulation <sup>b</sup>	Chézy, Manning, White-Colebrook	[0.05/3], [0.1/1]

<sup>a</sup>Tested user-defined model parameters are varied while all other run variables are held constant. Median and standard deviation are shown in brackets: [ $D_{50}/\text{Std}$ ]. For all runs skewness = 0.

<sup>b</sup>Select model parameters are tested using two grain-size distributions.

### **3.3. Parameter Space**

The parameter space explored in this study is defined by changes in the grain-size distribution of the sediment load entering the delta apex. I vary four aspects of the grain-size distribution (Table 2 and Figures 4b and 4c): (1) median grain size: the simplest value representing the caliber of the sediment load, (2) standard deviation: a value characterizing the sorting of the sediment load, (3) skewness: a value that determines whether the bulk of the sediment is larger or smaller in size than the mean grain diameter, (4) percent cohesive sediment: determines the bulk amount of cohesion within the system.

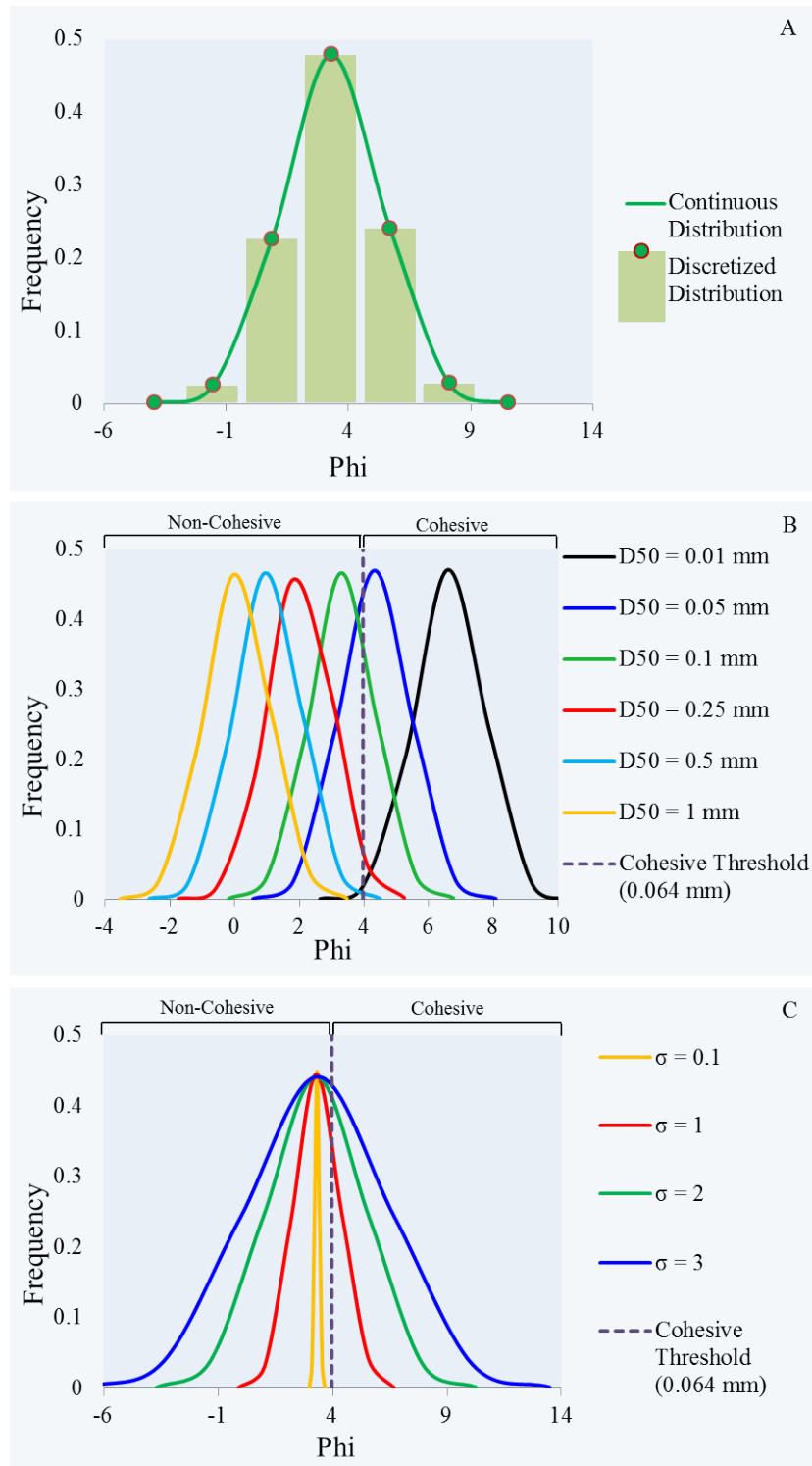


**Figure 4.** Example grain-size distributions showing (A) discretization of a continuous grain-size distribution into seven sediment fractions represented as a histogram (example shown for  $D_{50} = 0.1$  mm,  $\sigma = 2 \phi$ ), (B) the ranges in median grain sizes (examples shown for  $\sigma = 1 \phi$ ), and (C) the ranges in standard deviations (examples shown for  $D_{50} = 0.1$  mm). The location of Delft3D's cohesive grain size threshold is included for reference within phi space.

In this study I assume a unimodal, log-normal grain-size distribution (normal in phi space) for simplicity, although there is debate as to whether a bimodal or log-hyperbolic distribution is more common in natural river systems [e.g. *Hajek et al.*, 2010]. I start with a unimodal distribution because it is characterized by fewer parameters (i.e. one median, standard deviation, and skewness). This makes constraining cause and effect between the input grain-size distribution parameters and the output delta morphology metrics more straightforward than it would be if a multimodal distribution was used. In this study median grain size ( $D_{50}$ ) is varied from 0.01 mm (silt) to 1 mm (coarse sand), which is consistent with global deltaic systems [*Orton and Reading*, 1993; *Syvitski and Saito*, 2007]. Standard deviation ( $\sigma$ ) is calculated by the following formula [*Folk*, 1974]:

$$\sigma = \sqrt{\sum f_i (D_i - D_{50})^2} \quad (4)$$

where  $f_i$  is the weight percent of each  $i$ th sediment fraction and  $D_i$  is the size of each  $i$ th sediment fraction. Standard deviation of the distribution is varied (presented here with units of phi) from 0.1 (well sorted) to 3 (poorly sorted). Skewness ( $Sk$ ) is calculated as [*Folk*, 1974]:

$$Sk = \frac{\sum f_i (D_i - D_{50})^3}{100\sigma^3} \quad (5)$$

and is varied from -0.7 to 0.7 which encompasses varying degrees of fine and coarse skewed distributions as well as a normal Gaussian distribution (skewness = 0). For example, a positively skewed distribution (by phi value) corresponds to a “tail” that lies to the right of the distribution’s mean, or the finer grain size end. It follows that a positively skewed distribution will be composed of a higher volume of sediment below

the cohesive grain size threshold, and thus represents a more cohesive sediment input. Similarly, a negatively skewed distribution represents a sediment input characterized by a higher volume of larger grain sizes, and thus a less cohesive sediment load.

The variations in grain-size distribution parameters determine the fraction of sediment below the 64  $\mu\text{m}$  threshold for cohesive sediment in Delft3D (Figures 4b and 4c), resulting in different ratios of cohesive:non-cohesive sediment contributing to delta growth. These ratios are represented as a percentage of the total volume of sediment that is defined as cohesive (% cohesive) and range from 0% to 100% (Table 2), thus representing a full range in bulk sediment cohesion within the system. Although additional variables affect bulk sediment cohesion within natural systems (e.g. vegetation), I only consider the effect due to the mud:sand ratio.

The dependency of the cohesive:non-cohesive sediment ratio variations on the median, standard deviation, and skewness of the grain-size distribution makes it difficult to determine which of the four aspects exerts the strongest control on delta morphology. Despite this complication, it creates a suite of more realistic sediment loads capturing natural variations in grain sizes [*Orton and Reading, 1993; Syvitski and Saito, 2007*] and a full range of bulk cohesion.

#### **4. Results**

I conducted 33 runs of delta growth, each with a different grain-size distribution (Table 2, Figures 5 and 6). Deltas are compared at equivalent morphological times, defined as the time when the same volume of sediment has entered the system.

The key result of the 33 runs is that deltas undergo a morphological transition as the median of the grain-size distribution increases (Figures 5 and 7). At relatively small median grain size values deltas have elongate planform morphologies with shallow topset gradients and few distributary channels. On the other hand, deltas built by larger grain sizes exhibit semi-circular shapes with smooth shorelines, steep gradients, and many active channels.

In this section I explore this morphological transition by (1) describing how grain sizes change the dominant delta-building process, and (2) measuring four morphometric parameters (topset gradient, number of channel mouths at the delta shoreline, shoreline rugosity, and bulk delta shape) designed to quantify this morphological transition.

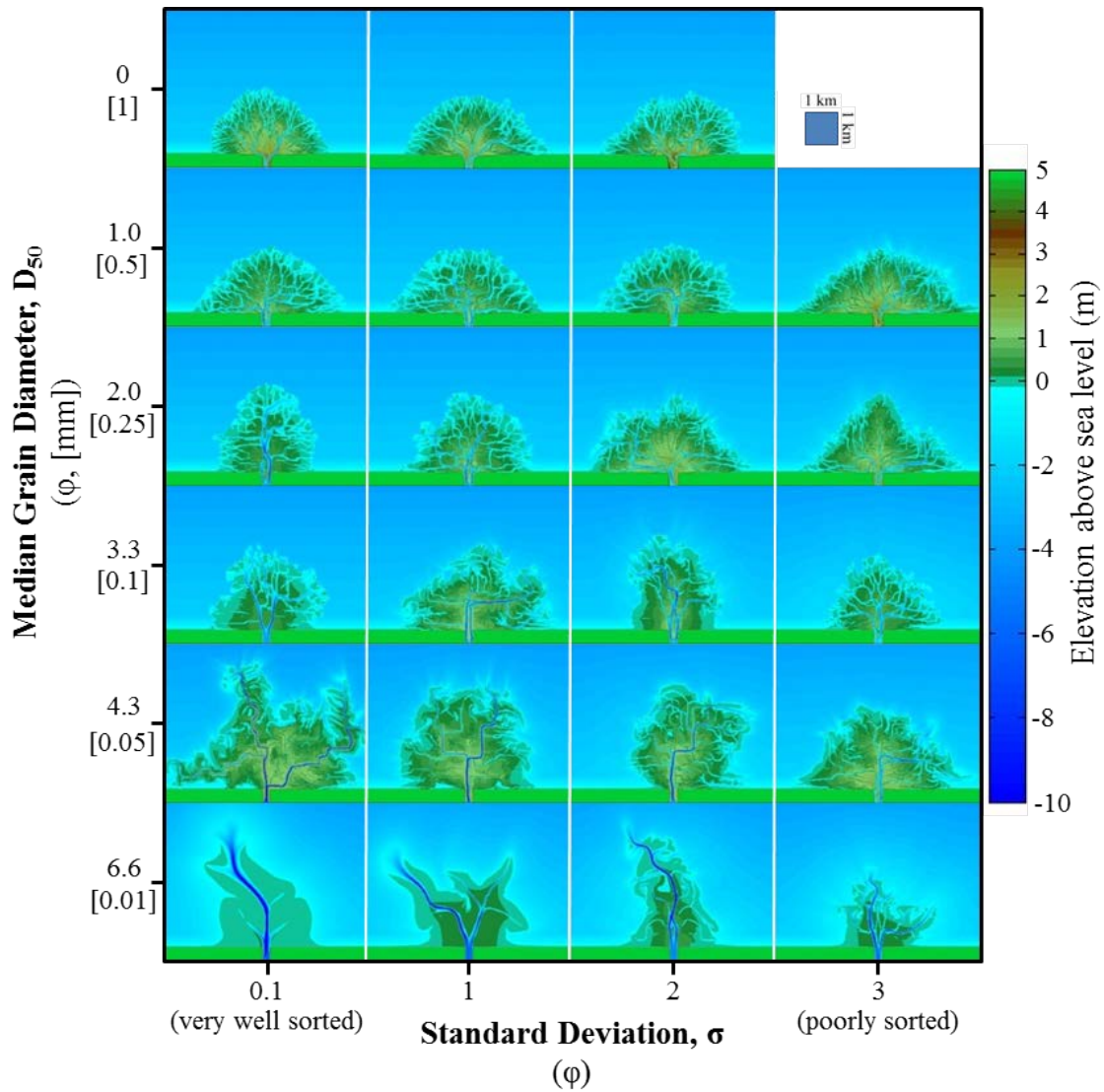


**Figure 5.** Delft3D model results that show different delta morphologies created from different grain-size distributions. Deltas are pictured when the same volume of sediment has entered the system. Median grain diameters (y-axis) are expressed in phi values with size in mm shown in brackets. Standard deviations are expressed in phi values. Note that both x- and y-axis intervals vary. For all runs skewness = 0.

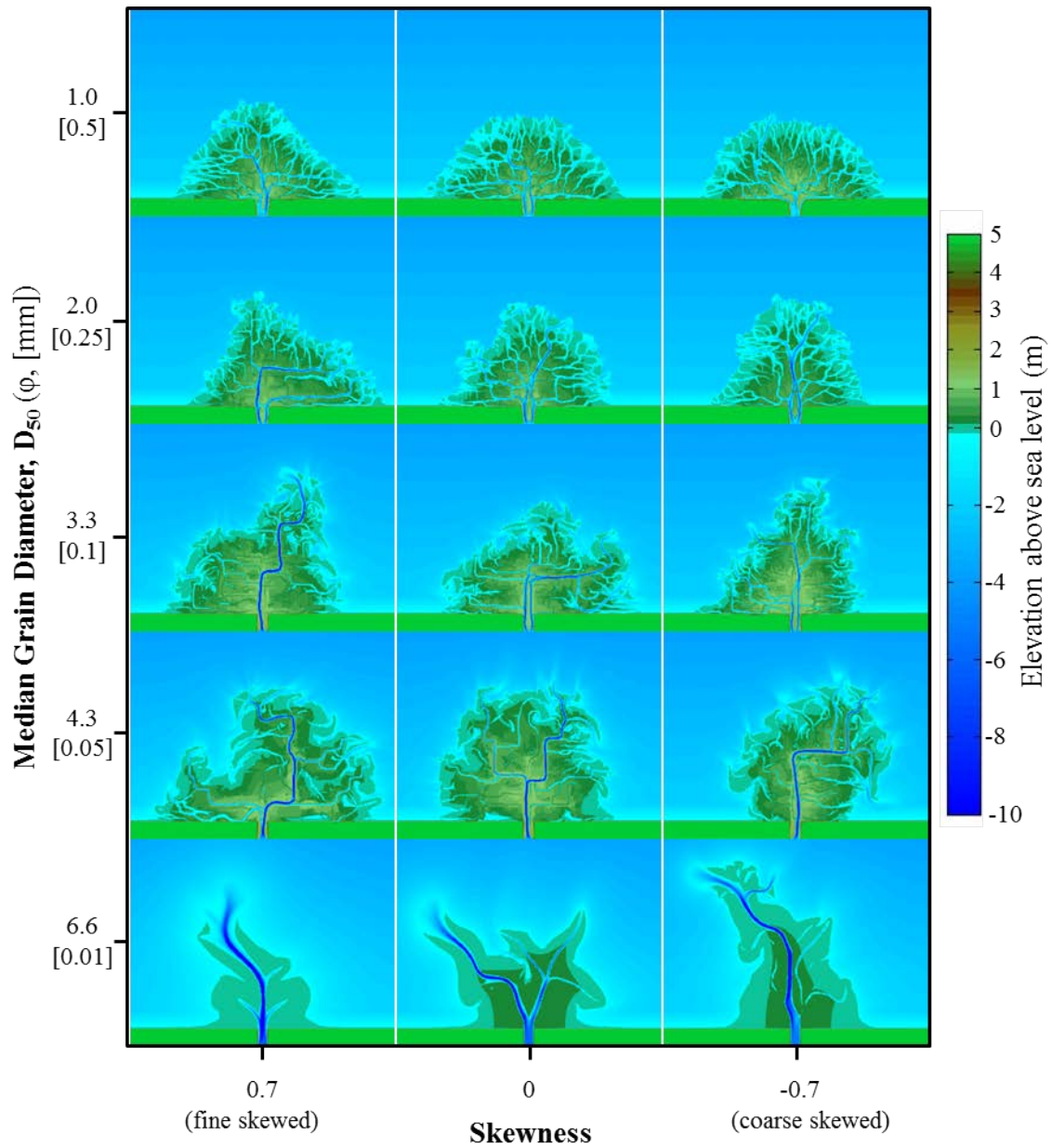


**Figure 6.** Model deltas under varying skewness of the grain-size distribution (x-axis) and median grain size (y-axis). The deltas in the middle column (skewness = 0) are the same results presented in Figure 5. Little to no morphological variation exists along the x-axis. Note that the y-axis intervals vary. For all runs  $\sigma = 1 \phi$ .

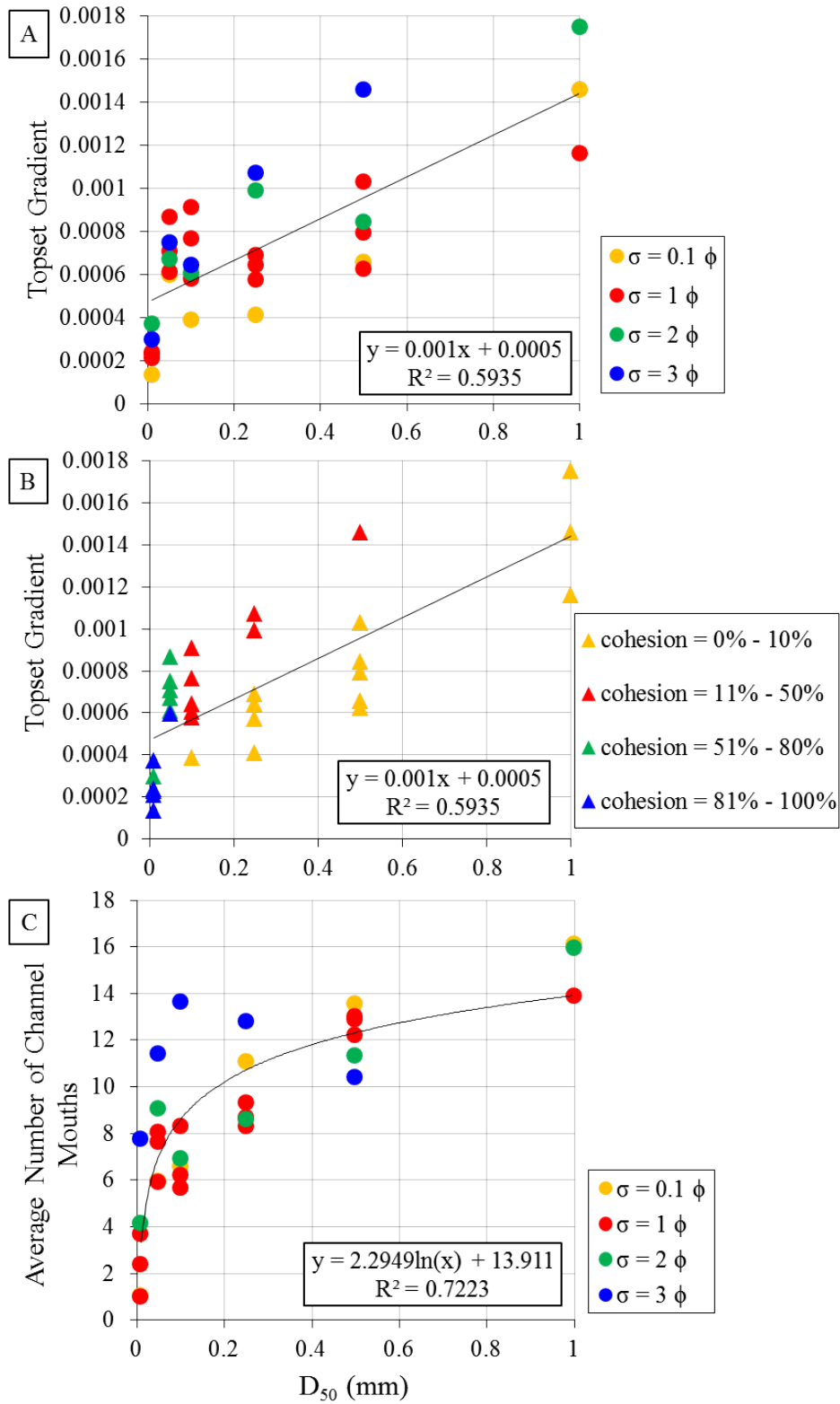


**Figure 7.** Relationship between median grain size and key morphometric parameters: (a) topset gradient (grouped by standard deviation); (b) topset gradient (grouped by percent cohesion); and (c) average number of channel mouths (grouped by standard deviation).

#### 4.1. Variation in Delta-Building Processes

Analysis of the time-evolution of delta growth indicates that these modeled deltas arise from delta-building processes also found in natural systems. In the model runs deltas are constructed by the following three deltaic processes: (1) levee growth and channel elongation, (2) river mouth bar construction and subsequent channel bifurcation, and (3) channel avulsions. The extent to which a given delta-building process dominates depends on the incoming grain sizes, and the dominance of certain delta-building processes is later shown to determine the resulting delta morphology.

Deltas built by smaller grain sizes are dominated by levee growth and subsequent channel elongation (Figures 8a-8c). As the stable levees prograde basinward (e.g. northwest channel in Figures 8b and 8c) few bifurcations around river mouth bars occur because the fine grains settle slowly and are advected over a broad area in front of the prograding mouth. This slows mouth bar construction. At intermediate grain sizes delta channel networks are dominated by bifurcations around river mouth bars (Figures 8d-8f). As mouth bars prograde, they create local shoreline deviations ~4-6 channel widths in length (e.g. arrows in Figures 8e and 8f). Coarse-grained deltas are dominated by mobile channels that avulse frequently (Figures 8g-8i), creating numerous flooding events that erode the floodplain and create a large number of channels.

These results indicate that changes in median grain size change the dominant delta-building process operating on the delta. In the next section I quantify the different delta morphologies that each of these grain-size distributions creates. Later I show how it is the relative balance of delta-building processes, as controlled by variations in the grain-

size distribution, which determines channel network morphology and delta planform morphology.

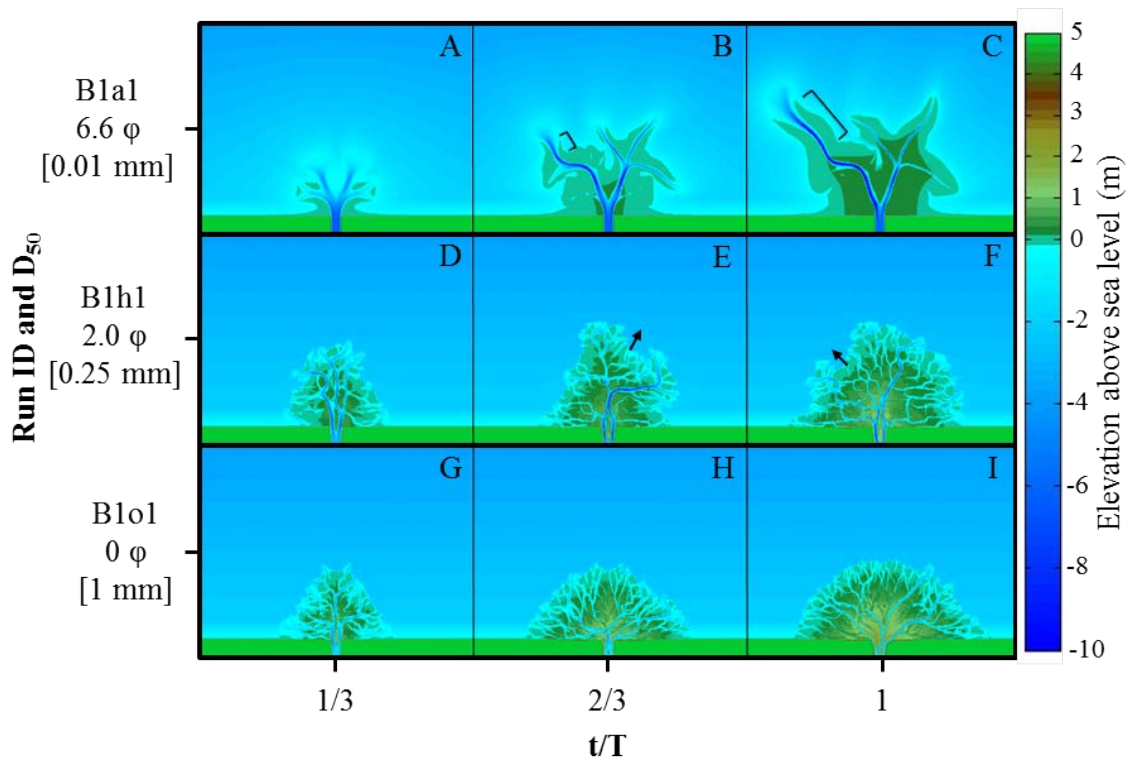


**Figure 8.** Evolution of fine (a-c), intermediate (d-f), and coarse (g-i) grained deltas. (b-c): brackets highlight northwest channel elongation. (e-f): arrows show shoreline deviations  $\sim 4$ -6 channel widths in length. The x-axis represents relative delta growth, where  $t$  is time and  $T$  is total time.  $T$  is calculated when a predetermined volume of sediment has entered the system. Runs shown here have  $\sigma = 1 \phi$  and skewness = 0.

#### 4.2. Variation in Delta Channel Network and Planform Morphology

Numerical results show that delta morphology varies as a function of the median and standard deviation of the grain-size distribution. This is evident by the qualitative observation that a morphological transition occurs within grain size parameter space as both median and standard deviation are increased (lower-left to upper-right of Figure 5). At low median grain size and standard deviation values (a silty, well sorted sediment

input), deltas have shallow topset gradients, few active channel mouths, smooth shorelines, and elongate planform morphologies. At high median grain size and standard deviation (a sandy, poorly sorted sediment input), deltas have steeper topset gradients, more active channel mouths, somewhat smooth shorelines, and semi-circular planform morphologies.

To further substantiate these observations I measure four morphometric parameters: topset gradient, number of channel mouths, shoreline rugosity, and bulk delta shape. These metrics are chosen because they highlight the differences among the observed end-member morphologies. Additionally, they are simple measurements that can be applied to any field delta, and measurement of number of channel mouths, shoreline rugosity, and bulk delta shape requires only a single aerial image. This ensures that conclusions based on these metrics can easily be applied to images of global deltas for comparison.

#### **4.2.1. Description of Morphometric Parameters**

To calculate these morphometric parameters I first classify all grid cells in the modeling domain as shoreline, open water, channelized topset, or land. I use the *Opening-Angle Method* (OAM) [Shaw *et al.*, 2008] to delineate the delta shoreline, which defines a grid cell as ‘seaward’ or ‘landward’ of the shoreline based on the angular swath that is ‘open’ to the ocean. The shoreline is then defined as the boundary between the two domains. For example, if a grid cell behind a large mouth bar cannot ‘see’ any open ocean it would be classified as landward of the shoreline. This permits an objective definition of the shoreline because it is otherwise difficult to decide if a detached mouth bar is part of the shoreline or how to draw the shoreline across open delta river mouths.

For all the grid cells marked as ‘landward’ I differentiate between those that are channelized and those that are unchannelized (i.e. land). Active channelized cells are defined by depth ( $D$ ), water velocity ( $u$ ), and total sediment flux thresholds ( $Q_t$ ), where  $D \geq 0.25$  m,  $u \geq 0.2$  m/s, and  $Q_t \geq 2.25 \times 10^{-4}$  m<sup>3</sup>/s (per 25 m cell). All remaining cells within the shoreline polygon that are not channelized are considered land.

To calculate delta topset gradient I measure rays from the delta apex to points along the shoreline spaced ~20 meters apart, and I assume a linear slope between the apex and shoreline points. The average of these values is used as a representative topset gradient.

A channel mouth is defined as those locations where there are two or more adjacent channelized cells that intersect the shoreline. The number of active channel mouths was measured throughout delta growth and the average of these values calculated after the delta reached a state of dynamic equilibrium, where the number of channel mouths no longer changes significantly with time. The number of active channel mouths at the delta shoreline is an important morphometric parameter for two reasons. First, the channel mouth represents the location where sediment is deposited at the shoreline and thus represents locations of localized shoreline progradation. Therefore, number and spacing of channel mouths should relate to shoreline rugosity and overall delta shape. Second, the number of channel mouths is the result of flow splitting within the delta topset, and thus is a simple quantitative representation of the channel network.

Shoreline rugosity is calculated as a sinuosity value, where the total delta shoreline length is normalized by the length of a smoothed, or “average”, shoreline location (Figure 9a). This measures local deviations from the “average” shoreline. A

large sinuosity measurement represents a very rugose shoreline characterized by larger-scale shoreline deviations.

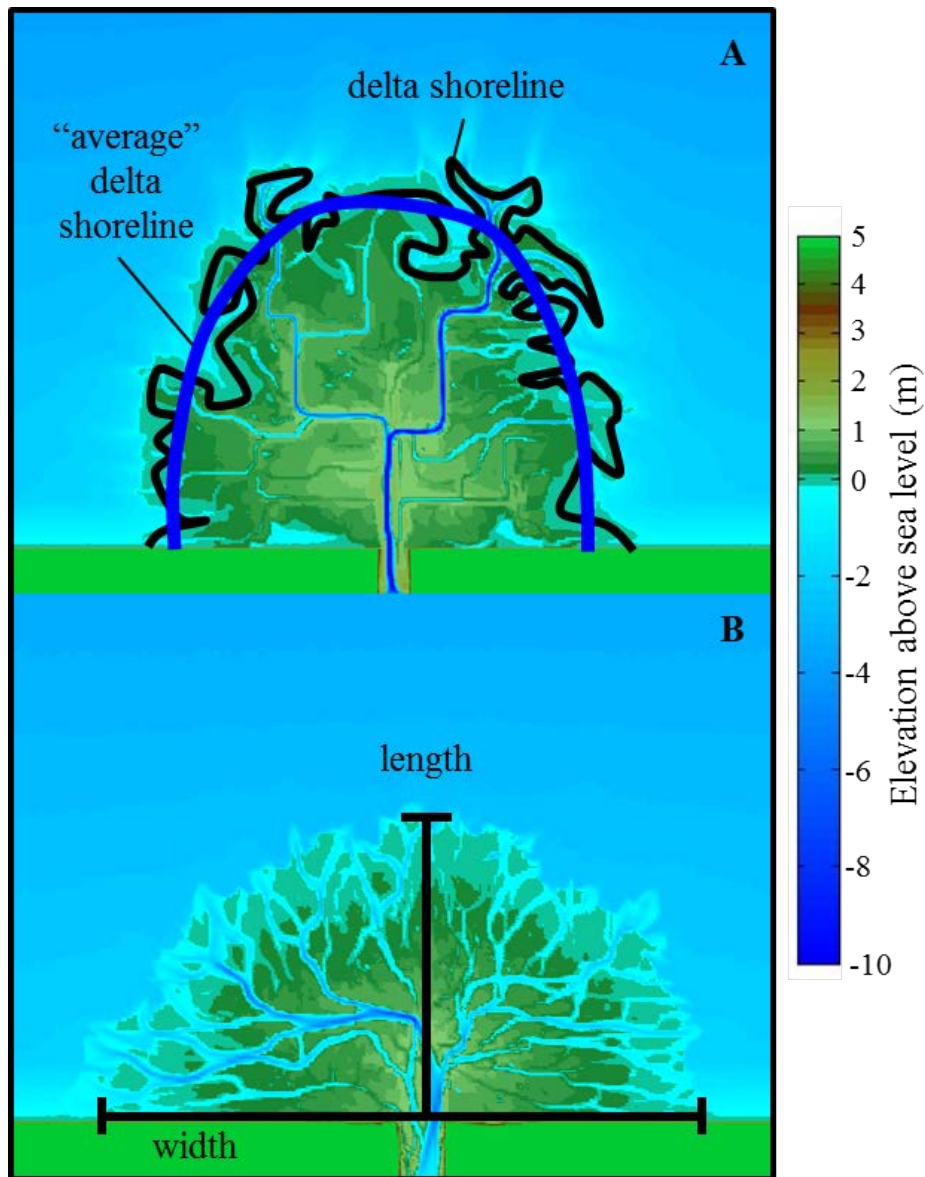


**Figure 9.** Cartoons depicting how (a) shoreline rugosity (Run ID = B1c1, rugosity value  $\approx 1.6$ ) and (b) bulk delta shape (Run ID = C1m1, bulk shape value  $\approx 0.9$ ) are measured. See text for description of calculations.

Changes in delta planform morphology are quantified with a simple bulk shape metric where  $X = W_d / 2L_d$ .  $W_d$  is delta width defined as the maximum, shore-parallel distance of the delta shoreline, and  $L_d$  is delta length defined as the maximum shore-perpendicular longitudinal distance from the delta apex to the furthest basinward shoreline point (Figure 9b). This ratio is divided by two so that deltas that have prograded equal amounts laterally and basinward of the delta apex ( $W_d \approx 2L_d$ ) have a bulk shape value of one. Deltas with  $X = 1$  resemble semi-circles and deltas with  $X < 1$  or  $X > 1$  are elongate with long axes perpendicular or parallel to the shore, respectively.

#### **4.2.2. Effect of Median Grain Size on Delta Channel Network and Planform Morphology**

Median grain size exerts the strongest control on delta morphology of the parameters considered in this study. While standard deviation of the grain-size distribution creates some variability in delta form (Figure 5) it is not as significant as median grain size. Skewness of the grain-size distribution has little effect on delta morphology (Figure 6). The following discussion will focus on the effect of median grain size on delta morphology.

Average topset gradient increases linearly as median grain size increases (Figures 7a and 10). Topset gradients vary an order of magnitude from  $1.4 \times 10^{-4}$  to  $2 \times 10^{-4}$  for the smallest median grain sizes to  $1 \times 10^{-3}$  to  $1.8 \times 10^{-3}$  for the largest median grain sizes. The spread in the relationship ( $R^2 = 0.59$ , significant at the  $P_N = 0.05$  level following Taylor, 1997) between median grain size and gradient is likely due to the effects of standard deviation (Figure 7a) and cohesion (Figure 7b), where deltas built by grain-size

distributions with larger standard deviations and higher percent cohesion tend to have steeper topset gradients.

The number of active channel mouths increases logarithmically with respect to median grain size (Figures 7c and 11). At low median grain size, deltas have 1-8 active channel mouths, whereas grain-size distributions with high median grain sizes create deltas with 13-16 active channel mouths. The correlation between median grain size and average number of channel mouths is strong ( $R^2 = 0.72$ , significant at the  $P_N = 0.05$  level following *Taylor, 1997*) and the spread in the data is likely due to standard deviation of the grain-size distribution. Deltas built by poorly sorted sediment inputs ( $\sigma = 3 \phi$ ) have a larger number of channel mouths than average (blue circles in Figure 7c).

Shoreline rugosity exhibits a non-monotonic relationship with respect to median grain size, where the most rugose shorelines are created by intermediate median grain sizes (Figure 12). At both low and high median grain sizes, rugosity values range from 1.34 to 1.49, indicating a smooth shoreline that deviates minimally from the average shoreline location. On deltas built by low median grain sizes, the development of river mouth bars is unlikely, which in turn decreases the local progradation at river mouths. Instead, the runaway progradation of only a few channels dominates the smooth shoreline development (e.g. Figure 8c). Similarly, delta shorelines built by high median grain sizes are also smooth because of the absence of localized progradation at individual channel mouths (e.g. Figure 8i). The highest rugosity values of  $\sim 1.57 - 1.62$  are measured on deltas built by low-intermediate median grain sizes and low standard deviation ( $D_{50} = 0.05 - 0.1 \text{ mm}$ ,  $\sigma = 0.1 - 1 \phi$ ). Based on inspection of the data this high rugosity value is

linked to local progradation at river mouths due to bar and levee development (Figures 8e and 8f).

Bulk delta shape increases with respect to median grain size (Figure 13). At low median grain sizes, deltas exhibit bulk shape values ranging from 0.3 to 0.5  $X$ , indicating that the planform morphologies are elongate and deviate from that of a semi-circle. High median grain sizes have bulk shape values closest to one, and thus approximate a semi-circle.

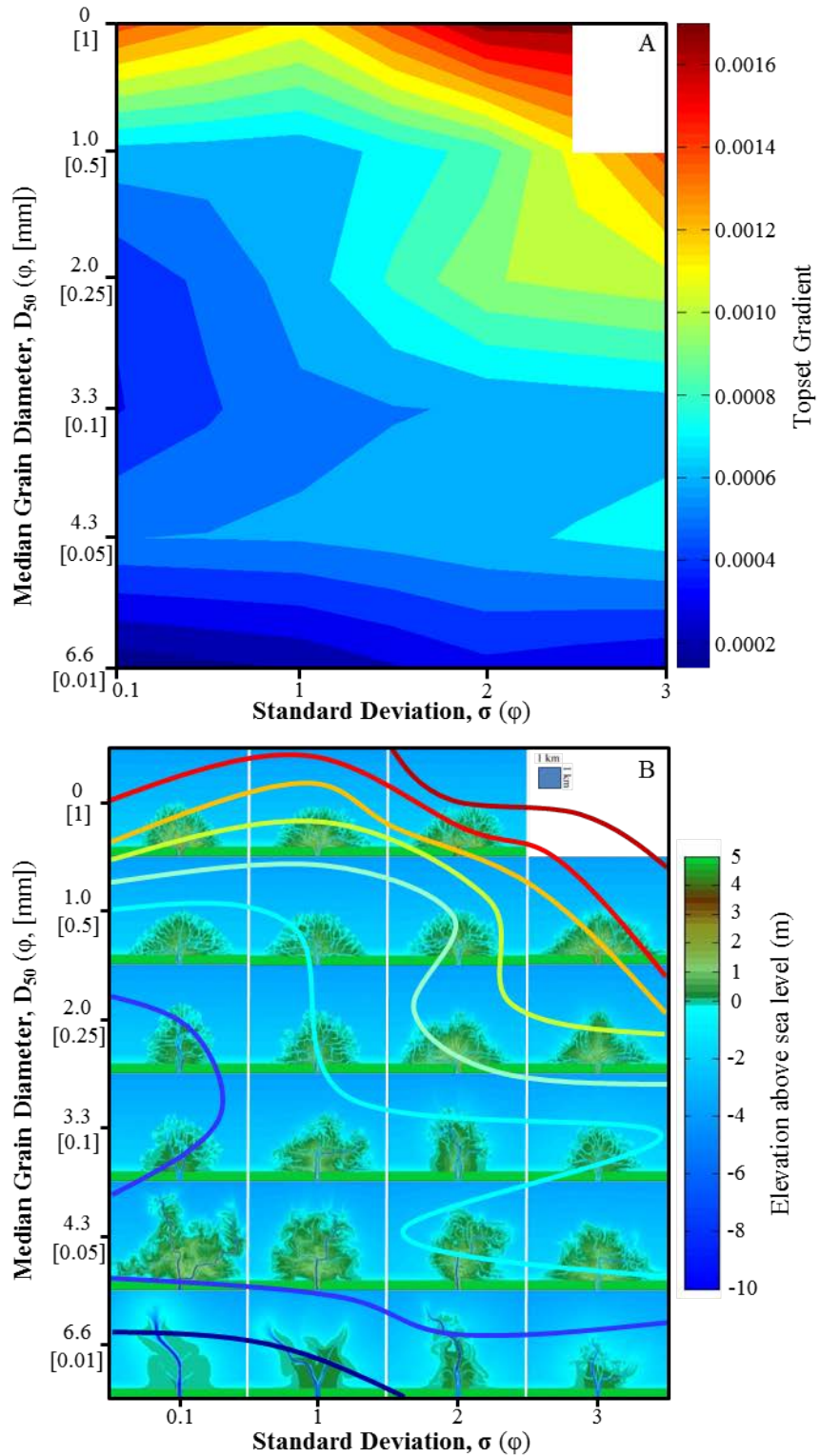


**Figure 10.** Measured topset gradients (a) contoured in the  $D_{50}$  vs.  $\sigma$  parameter space, and (b) with the contours from (a) superimposed on the images of model deltas.

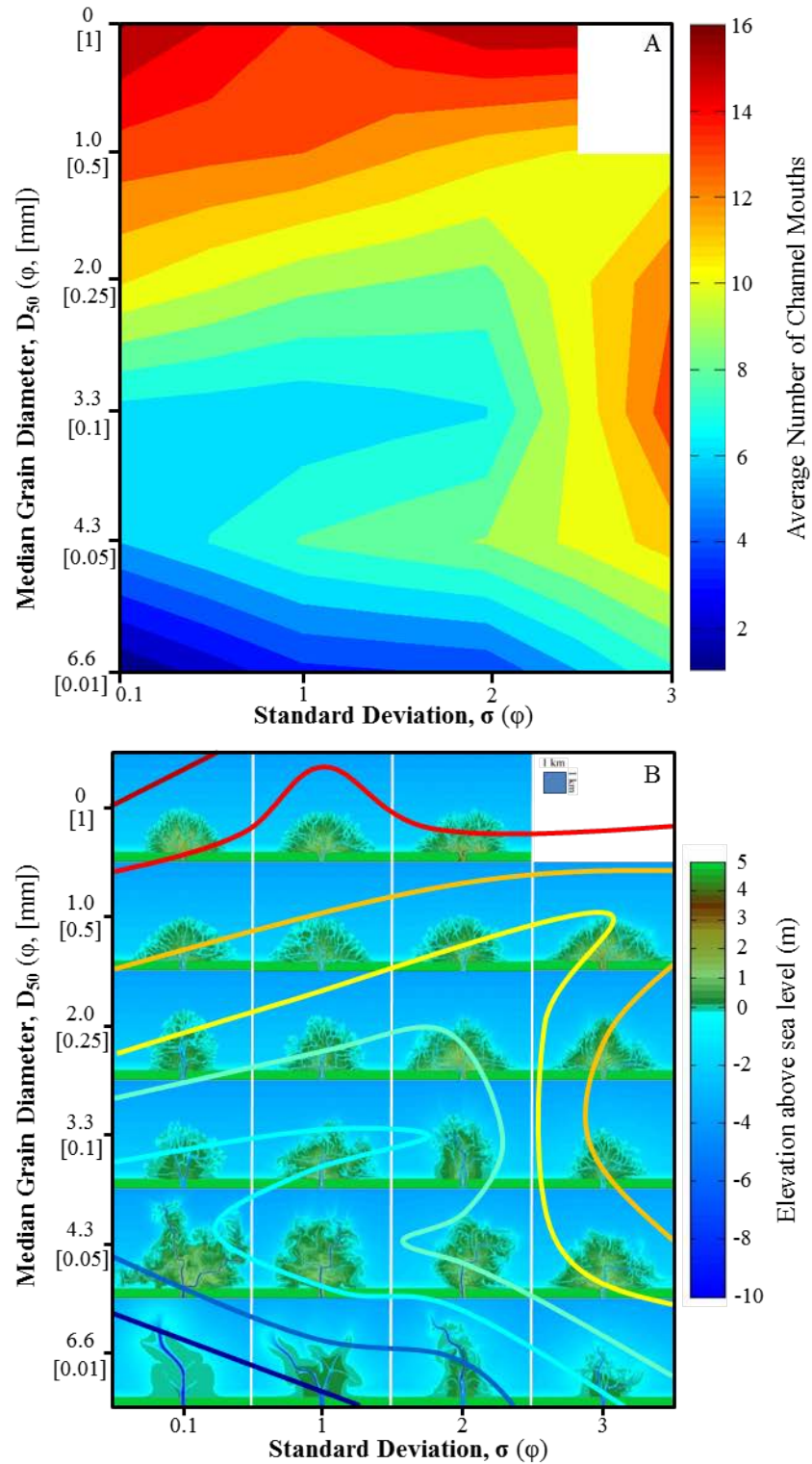


**Figure 11.** Measured average number of channel mouths (a) contoured in the  $D_{50}$  vs.  $\sigma$  parameter space, and (b) with the contours from (a) superimposed on the images of model deltas.

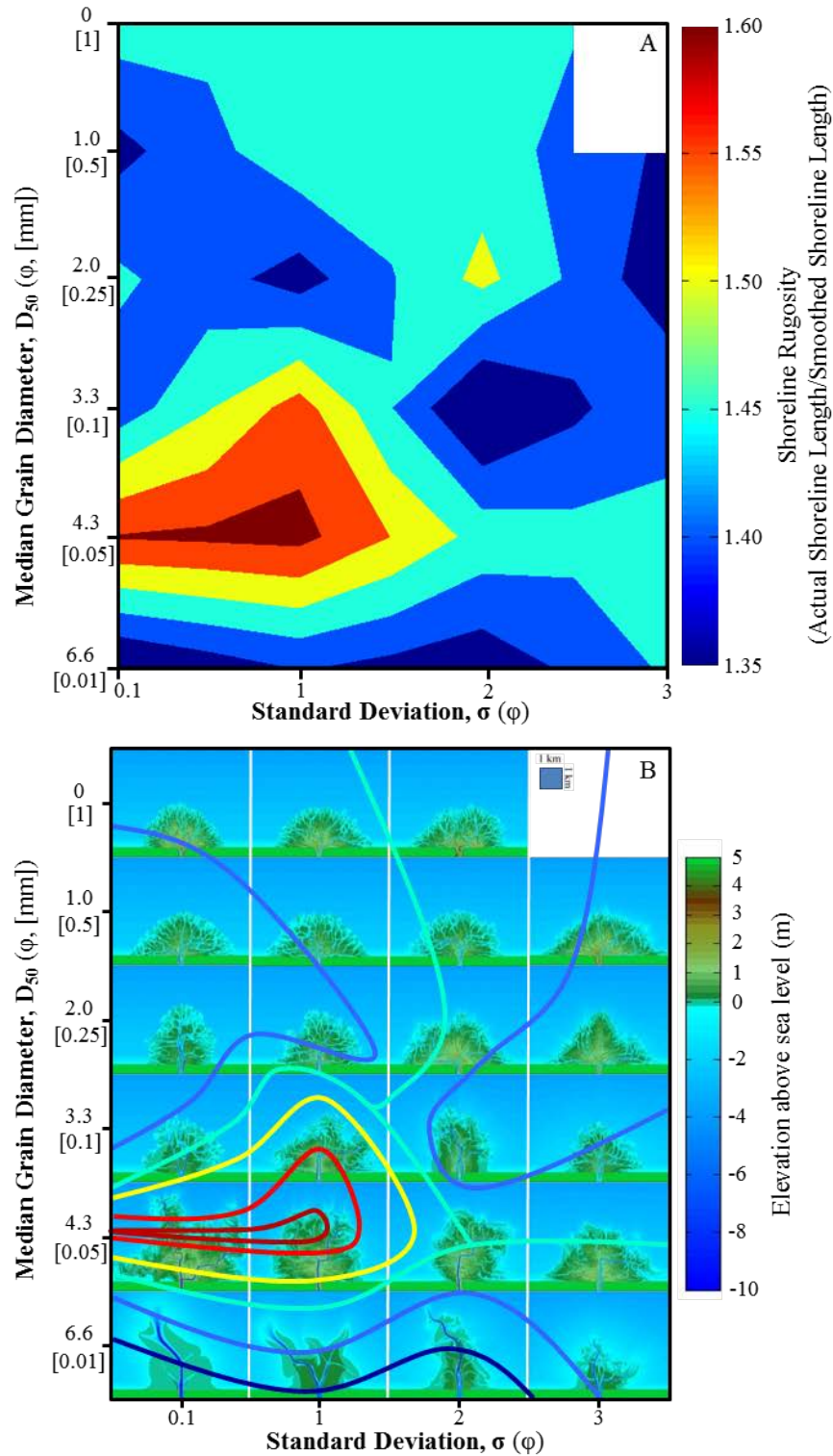


**Figure 12.** Distribution of measured shoreline rugosity, calculated as shoreline sinuosity (actual shoreline length / smoothed shoreline shape), (a) contoured in the  $D_{50}$  vs.  $\sigma$  parameter space, and (b) with the contours from (a) superimposed on the images of model deltas.

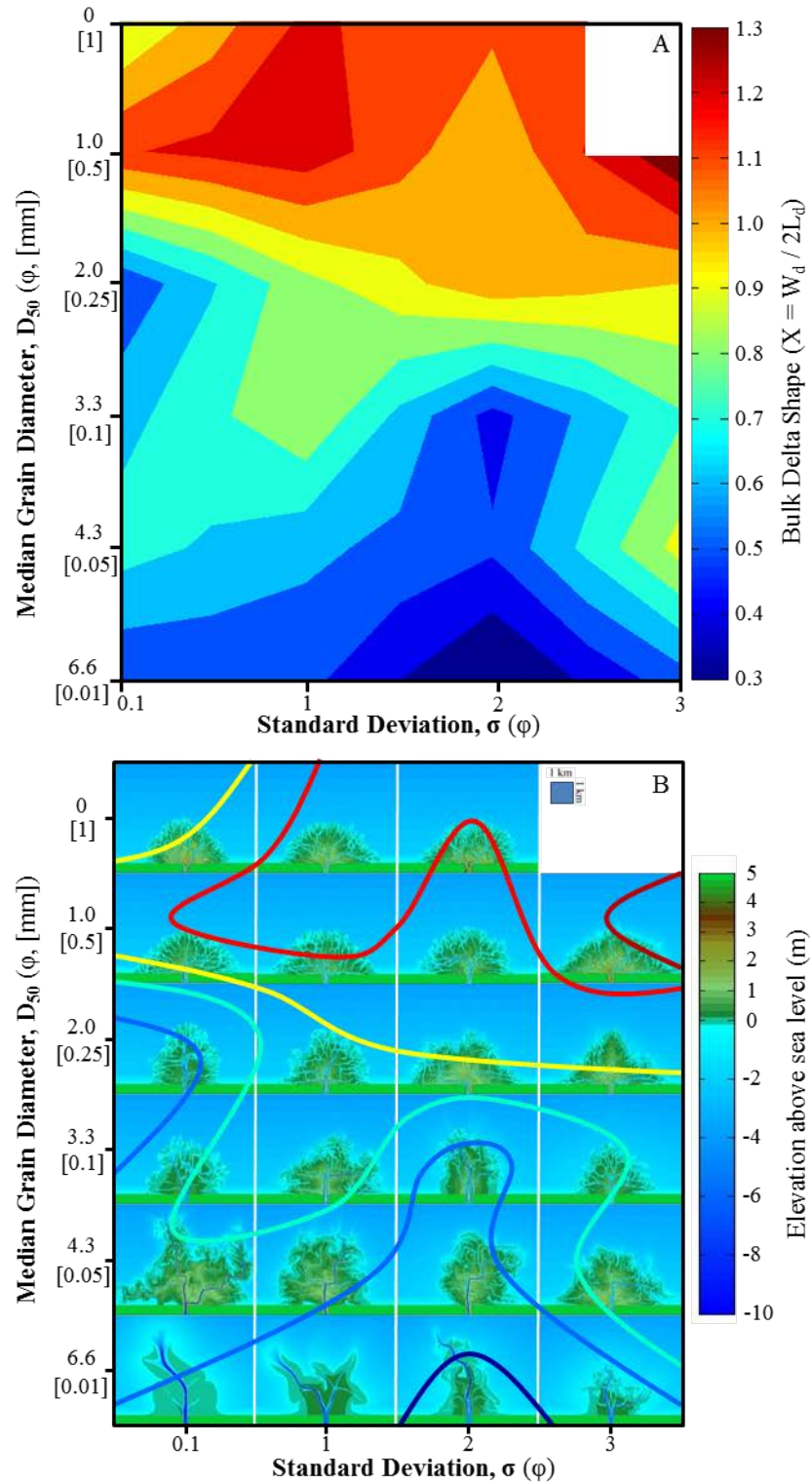


**Figure 13.** Distribution of measured bulk delta shape, calculated as  $X = W_d / 2L_d$ , (a) contoured in the  $D_{50}$  vs.  $\sigma$  parameter space, and (b) with the contours from (a) superimposed on the images of model deltas.

### 4.2.3. Effect of Cohesion on Delta Channel Network and Planform Morphology

The amount of cohesive sediment entering the domain varies as a result of changing the median, standard deviation, and skewness of the incoming grain-size distribution (Table 2, Figures 4b, 4c, and 14). The percent cohesive sediment ranges from 100% for small median grain sizes to 0% for large median grain sizes.

Topset gradient and percent cohesive sediment exhibit an overall negatively linear relationship (dotted line in Figure 15a). This relationship ( $R^2 = 0.30$ , significant at the  $P_N = 0.05$  level following *Taylor, 1997*) is likely due to the fact that higher bulk cohesions are created by lower median grain sizes, and the observed decrease in topset gradient is actually due to decreased median grain sizes (Section 5.1). However, for low bulk cohesions (0% - 50% cohesive sediment), an increase in cohesion for a given median grain size steepens the topset gradient (relationships for  $D_{50} = 0.25$  and 0.5 mm are significant at the  $P_N = 0.05$  level following *Taylor, 1997*) (left side of Figure 15a). The opposite is true for high bulk cohesions (50% - 100% cohesive sediment), where negative linear trends suggest an increase in cohesion for a given median grain size creates shallower topset gradients.

The average number of channel mouths decreases as percent cohesion increases ( $R^2 = 0.56$ , significant at the  $P_N = 0.05$  level following *Taylor, 1997*) (dotted line in Figure 15b), though the relationship is non-monotonic (black line in Figure 15b). Deltas with cohesive sediment inputs have the highest number of channel mouths (7-12) when the sediment input is ~70% - 80% cohesive, and fewer channel mouths (1-6) when bulk cohesion is either lower (~40% - 70%) or higher (~80% - 100%) (right side of Figure

15b). As sediment inputs become non-cohesive (0% - 40%) there is an increase in number of channel mouths (6-16).

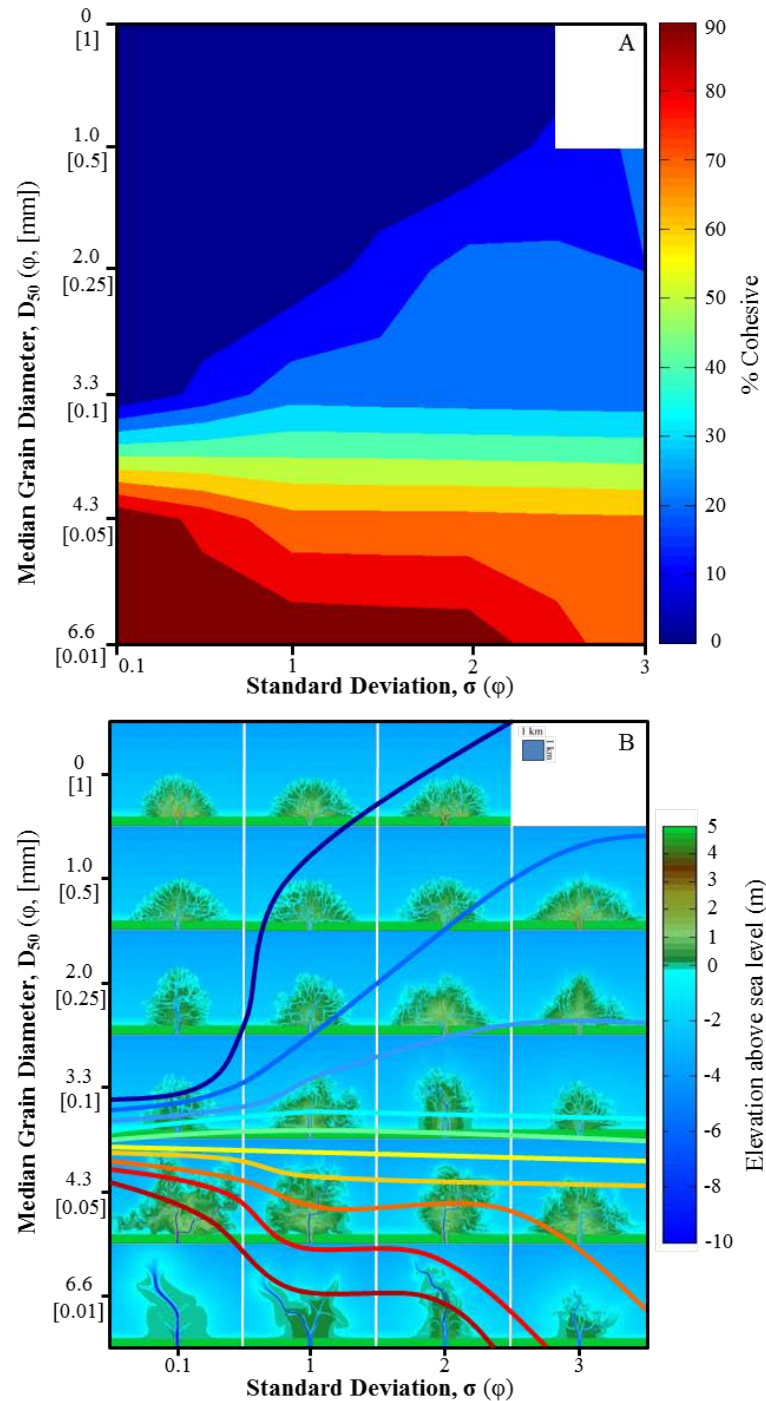


**Figure 14.** Percent cohesive sediment that makes up the incoming sediment load (a) contoured in the  $D_{50}$  vs.  $\sigma$  parameter space, and (b) with the contours from (a) superimposed on the images of model deltas.

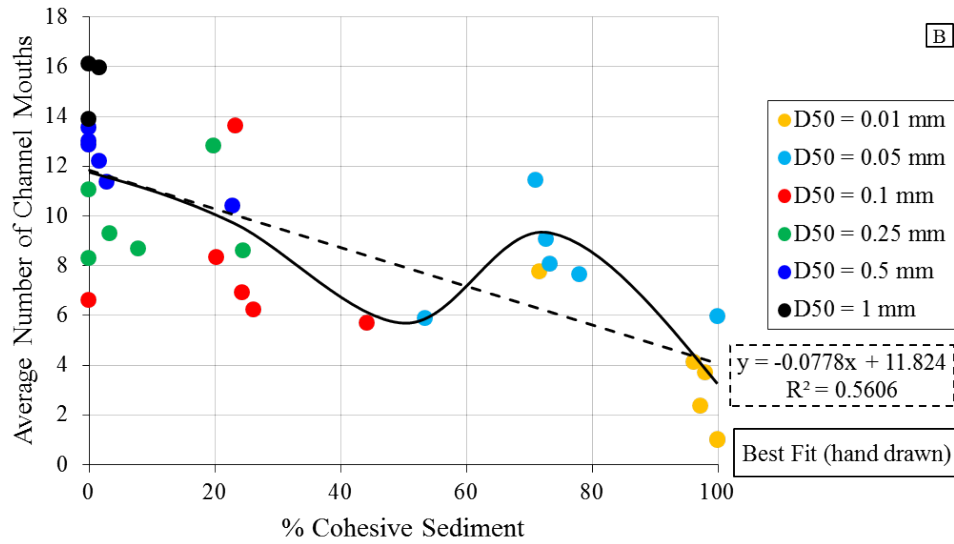
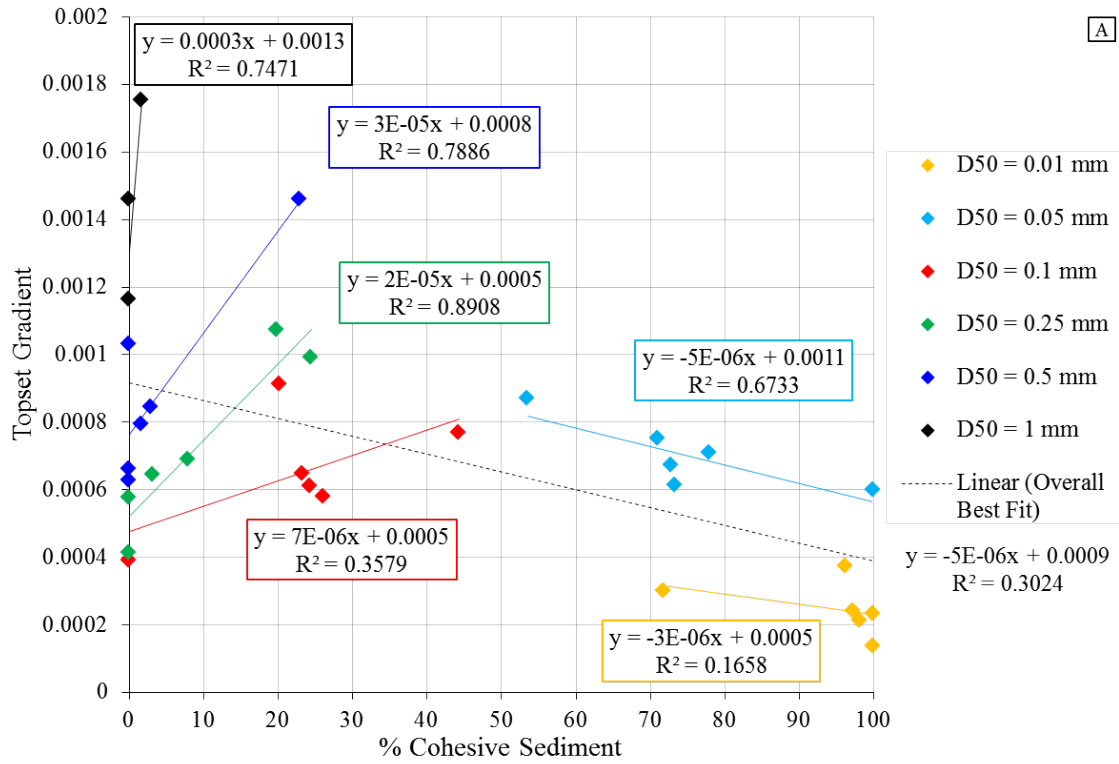


**Figure 15.** Relationship between percent cohesive sediment and (A) topset gradient, and (B) average number of channel mouths. Colors denote median grain size.

## 5. Discussion

In this section I show how changes in the grain-size distribution set the dominant delta-building processes that produce variations in channel network morphology and delta planform morphology. The final product is a process-based model for grain size effects on delta morphodynamics.

### 5.1. Does Median Grain Size Control Topset Gradient?

The results of the analyses in this thesis indicate that an increase in median grain size leads to a linear increase in delta topset gradient (Figures 7a and 7b) and is likely the dominant factor controlling topset gradient. What controls this relationship?

Assuming steady and uniform flow, the equilibrium topset gradient can be predicted as a function of varying sediment flux and median grain size. Equations for steady and uniform flow (6-8) and a sediment transport relation (9) are combined into equation (10), which relates the incoming median grain size to the equilibrium bed surface gradient required to transport the grains. The sediment transport relation assumes the excess bed shear stress is significantly larger than the critical bed shear stress required for sediment transport, a value that is small for sand systems.

$$Q = uDB \quad (6)$$

$$\tau_0 = \rho_w gDS \quad (7)$$

$$u = C\sqrt{RS} \quad (8)$$

$$q_t = \alpha(\theta_0)^p \sqrt{\left(\frac{\rho_s}{\rho_w}\right) g D_{50}^3} \quad (9)$$

$$S = K \sqrt{\frac{q_t}{q^2} D_{50}^{3/2}} \quad (10)$$

$B$  is channel width (m),  $\tau_0$  is bed shear stress ( $\text{N/m}^2$ ),  $S$  is the equilibrium gradient,  $q_t$  is total sediment flux per unit width ( $\text{m}^2/\text{s}$ ),  $a$  and  $p$  are constants used in the sediment transport relation, and  $q$  is water discharge per unit width ( $\text{m}^2/\text{s}$ ). When equations (6-9) are combined to form equation (10), the remaining constant  $K$  is a function of roughness, gravity, and density.

Using values of water and sediment discharge from the numerical experiments, I calculate the predicted gradient ( $S$ ) that should result as a function of varying sediment load and median grain size (Figure 16). Observed spread of the predicted vs. measured topset gradient around the line of perfect agreement is due to standard deviation of the grain-size distribution. This trend suggests that a delta increases its slope to create higher bed shear stresses in order to transport larger grain sizes and sediment fluxes, as has been similarly observed for alluvial fans [Whipple *et al.*, 1998].

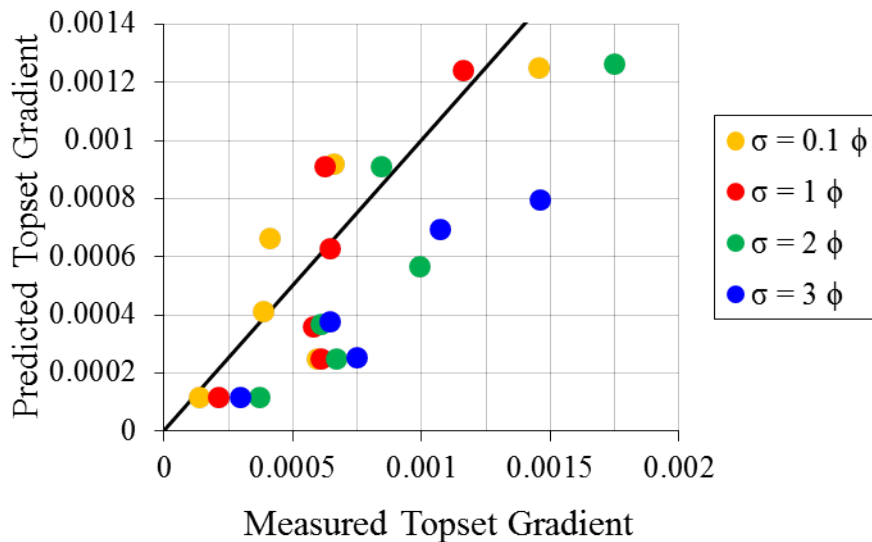


**Figure 16.** Predicted topset gradients ( $S$  in equation 10) vs. measured topset gradients. Black line denotes perfect agreement.

In all runs, topset gradient reaches a dynamic equilibrium (Figure 17). Steeper topset gradients created by coarser grain sizes require higher aggradation rates (per unit length of progradation) to maintain dynamic equilibrium. It has been previously shown that increased aggradation rates on delta topsets lead to more mobile channels [Martin *et al.*, 2009] which is likely the cause of increased channel mobility observed on coarse-grained deltas in this study (Figures 8g-8i) and may relate to the increase in number of channel mouths on coarse-grained deltas (Figures 7c and 11).

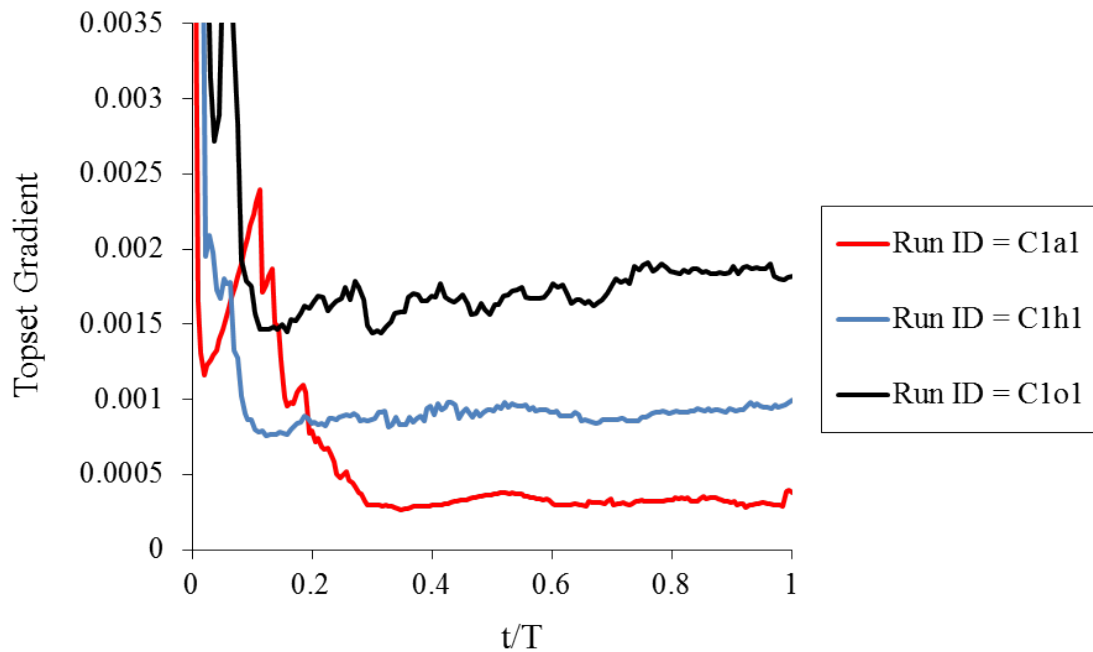


**Figure 17.** Measured topset gradient throughout delta growth shows topset gradient reaches a dynamic equilibrium after  $t/T$  of  $\sim 0.1$  for C1h1 and C1o1, and after  $t/T$  of  $\sim 0.3$  for C1a1. Representative examples shown for fine (C1a1,  $D_{50} = 0.01$  mm), intermediate (C1h1,  $D_{50} = 0.25$  mm), and coarse (C1o1,  $D_{50} = 1$  mm) grained deltas. The x-axis represents relative delta growth, where  $t$  is time and  $T$  is total time. Runs shown here have  $\sigma = 2 \phi$ .

## 5.2. How Does Median Grain Size Control the Number of Channel Mouths?

Sediment loads with larger median grain sizes create deltas with more channel mouths (Figures 7c and 11). Channels on a delta can be created by three processes: (1) bifurcation around river mouth bars, (2) bifurcation around braid bars initiated within the channel rather than at the channel mouth, and (3) avulsion to new locations and creation of crevasse channels. Channel avulsion and crevassing is typically associated with aggrading river systems [*Slingerland and Smith, 2004*] because the aggradation perches the channel above the floodplain, creating a gravitationally unstable channel that will seek the steeper and lower path in the adjacent floodplain. I suggest that the higher aggradation rates on coarse-grained deltas (as inferred from Figure 17 and from the higher elevations at the delta apex in Figure 5) create frequently avulsing channels with morphologies similar to crevasse channels.

To test this idea, I measure an average channel-switching time scale ( $\overline{T_{ch}}$ ) once delta growth has reached a state of dynamic equilibrium where the number of channel mouths and topset gradient (Figure 17) no longer change with time. Although the average number of channel mouths is constant through time, individual channels are mobile – they are abandoning their initial channel mouth locations for new locations on the delta topset. As previously described, a channel is defined by channelized grid cells (see Section 4.2 for threshold requirements). A channel's abandonment is thus defined by the abandonment of its channelized grid cells as they become inactive over time. As I will show later (Figure 18, Equation 15), channelized grid cells abandon at a rate that can be fit with an exponential decay function. I measure  $\overline{T_{ch}}$  by calculating an average channelized grid cell decay rate constant and then converting that to an average channel

lifetime. I use a decay constant to estimate  $\overline{T_{ch}}$  instead of directly measuring the average channel lifetime because the channels in some runs abandon slowly and persist for the entire time while the delta is at dynamic equilibrium. With a decay constant I can estimate the lifetimes of channels that abandon slowly beyond what is recorded in the model output.

A direct measurement of the channel-switching time scale is calculated as:

$$\overline{T_{ch}} = \tau \cdot \overline{B_{cells}} \quad (11)$$

where  $\tau$  is the mean lifetime of a channelized grid cell and  $\overline{B_{cells}}$  is mean channel width in number of grid cells for a given numerical experiment.  $\tau$  is calculated from the decay rate constant ( $\lambda$ ), where:

$$\tau = \frac{1}{\lambda} \quad (12)$$

Once the delta reaches dynamic equilibrium, a representative value for  $\lambda$  is obtained for each experiment by tracking the newly channelized grid cells that represent new channels as they decay through time. I mark the location of every newly channelized grid cell not associated with an existing channel (i.e. excluding those created by channel progradation) throughout the rest of the delta's lifetime. I then track the decay of those newly channelized grid cells (as they become inactive, or no longer meet the active channelization threshold requirements stated in Section 4.2) (Figure 18). At any time  $i$  following channel initiation, the total number of initially 'active channel cells' ( $C_{ch,0}$ ) will be:

$$C_{ch,0} = C_{ch,i} + C_{a,i} \quad (13)$$

where  $C_{ch,i}$  is the number of initially 'active channel cells' that have remained continually active by time  $i$ , and  $C_{a,i}$  is the number of those initially 'active channel cells' that have

been abandoned by time  $i$ . The fraction of  $C_{ch,0}$  that remains active by time  $i$  is measured as the ratio  $R_{ch}$ :

$$R_{ch} = \frac{C_{ch,i}}{C_{ch,0}} \quad (14)$$

which decays over time. It follows that a delta with a rapid decline in  $R_{ch}$  (solid black line in Figure 18) has channelized cells that are abandoned quickly after formation.

Deltas with  $R_{ch}$  values that decline slowly (solid red line in Figure 18) have relatively stable channelized cells.

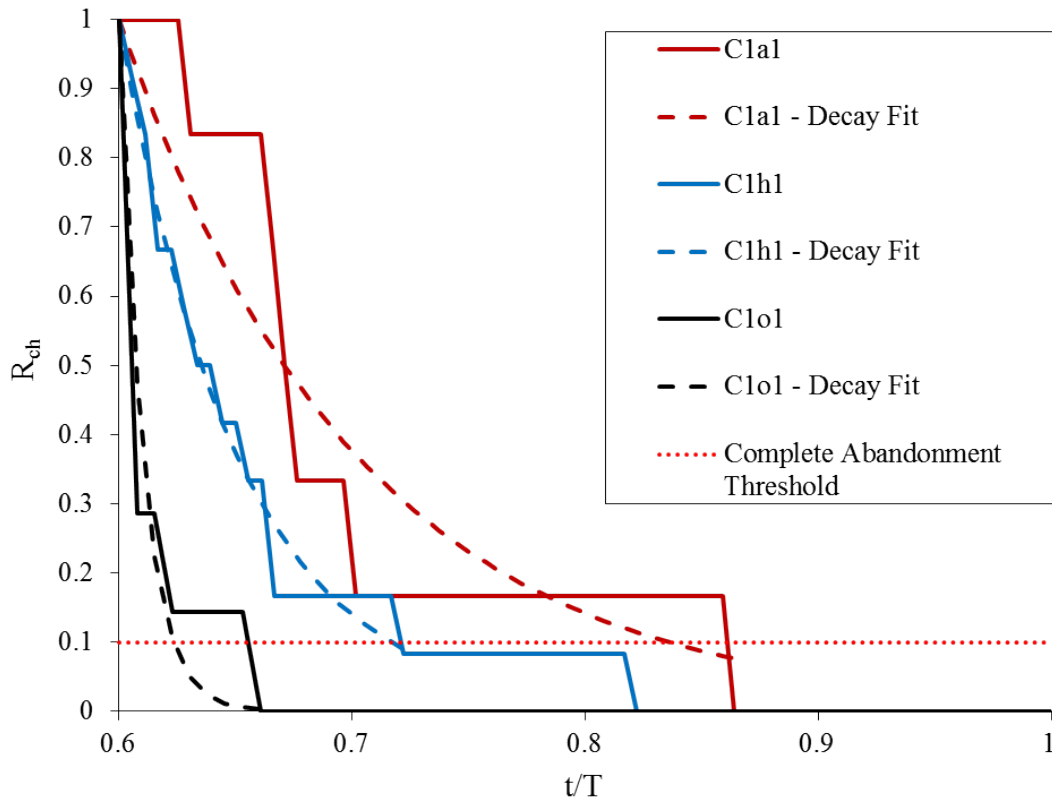


**Figure 18.** Ratio of channelized grid cells that are still ‘active’ after channel initiation ( $R_{ch}$ ) (solid lines) and decay curves fit to each abandonment rate (dashed lines). Examples shown here are for channels that formed at  $t/T = 0.6$ , where  $t$  is time and  $T$  is total time. Thus,  $t/T = 0.6$  corresponds to  $i = 0$  in this case. Complete abandonment is defined as the abandonment of 90% of the initially active channel cells, shown here as a dotted line. Examples shown for fine (C1a1,  $D_{50} = 0.01$  mm), intermediate (C1h1,  $D_{50} = 0.25$  mm), and coarse (C1o1,  $D_{50} = 1$  mm) grained deltas. Runs shown here have  $\sigma = 2$   $\varphi$ .

The abandonment of channelized grid cells through time is fit with an exponential decay function (dashed lines in Figure 18). This function has the form

$$R_{ch} = e^{-\lambda \cdot i} \quad (15)$$

where  $\lambda$  is the decay rate, and  $i$  is the time since channel formation (years). I define ‘complete abandonment’ as the abandonment of 90% of the initial ‘active channel cells’ (red dotted line in Figure 18). The decay rate is converted to  $\overline{T_{ch}}$  using equations (11 and 12).

Increasing median grain size leads to deltas with smaller  $\overline{T_{ch}}$  values. Fine-grained deltas, on the other hand, create stable channels that have much larger  $\overline{T_{ch}}$  values. This negative correlation between  $\overline{T_{ch}}$  and grain size arises because the faster aggradation rates needed to maintain steeper topset gradients in coarse-grained deltas lead to more frequent channel-switching. In all runs topset gradient reaches a dynamic equilibrium that increases with increasing grain size (Figure 17). To maintain a steeper gradient, a delta’s topset must aggrade at a faster rate (per unit length of progradation). The majority of aggradation in fluvial systems occurs in or near channels [*Heller and Paola, 1996; Törnqvist and Bridge, 2002*], which leads to superelevation of the channel relative to the adjacent floodplain, and subsequent channel avulsion [*Mohrig et al., 2000*]. *Jerolmack and Mohrig [2007]* show that a theoretical channel avulsion time scale,  $T_A$  (years), may be predicted as:

$$T_A = \frac{\overline{D}}{v_A} \quad (16)$$

where  $\overline{D}$  is average channel depth (m) and  $v_A$  is channel aggradation rate (m/yr). This relation accurately predicts measured avulsion time scales for natural systems [*Jerolmack and Mohrig, 2007*]. Using equation (16), I calculate theoretical channel avulsion time

scales ( $T_A$ ) for all 33 delta runs in this study by measuring in-channel aggradation rates and average channel depth near the delta apex (Figure 19).

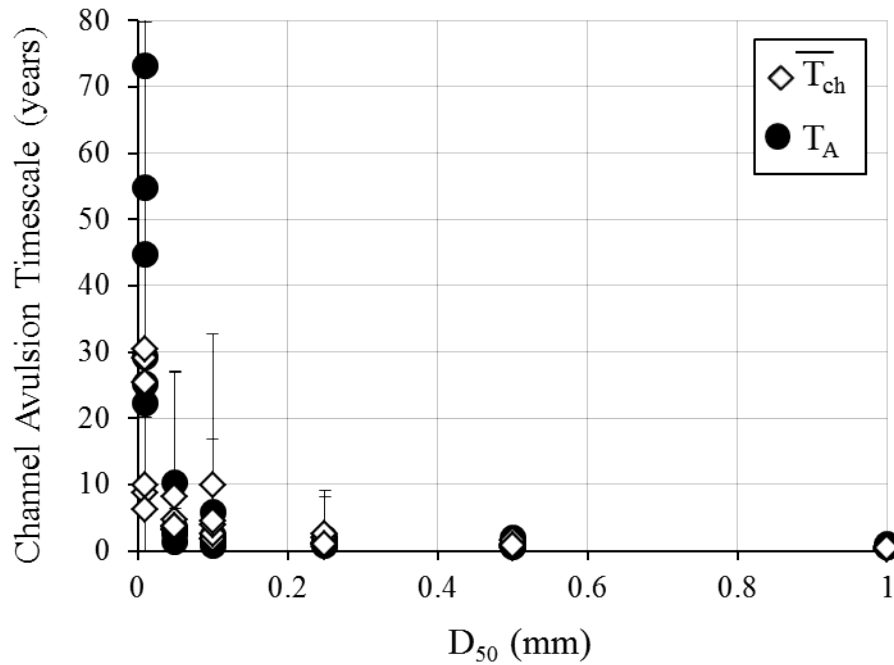


**Figure 19.** Measured  $\overline{T}_{ch}$  values and theoretical  $T_A$  values plotted against median grain size ( $D_{50}$ ).  $T_A$  is a theoretical avulsion frequency based on average channel depth and aggradation rates, and  $\overline{T}_{ch}$  is measured channel-switching frequency. Vertical bars on  $\overline{T}_{ch}$  represent measured standard deviation. See text for description of calculations.

Theoretical avulsion time scales ( $T_A$ ) exhibit a negative, non-linear relationship with median grain size that is similar to the relationship between measured channel-switching time scales ( $\overline{T}_{ch}$ ) and median grain size (Figure 19). Channel-switching on a delta may occur by either channel avulsion or lateral channel migration. I interpret  $\overline{T}_{ch}$  to be representative of a channel avulsion time scale. This interpretation is based on the remarkable similarity between measured  $\overline{T}_{ch}$  values and theoretical avulsion time scales ( $T_A$ ), and qualitative observation of channel movement by avulsion rather than lateral

migration (Figures 8g-8i). Theoretical  $T_A$  values are on average 1.3 times larger than measured  $\overline{T_{ch}}$  values, predicting that the channel avulsion time scale should be longer than observed in the model. This offset is due to the fact that the  $T_A$  formulation of equation (16) assumes that a channel must aggrade an entire channel depth above the adjacent floodplain before avulsing, whereas inspection of my model results suggests that channel avulsions often occur before this threshold is met. Despite the offset, the negative relationship between both  $T_A$  and  $\overline{T_{ch}}$  with median grain size suggests that increased aggradation rates on coarse-grained deltas cause superelevation of channels relative to the adjacent floodplain, which leads to more frequent channel avulsions.

Increased channel avulsion frequency should lead to a channel network with multiple simultaneously active channels [*Makaske, 2001; Jerolmack and Mohrig, 2007*], explaining the increase in number of observed channel mouths on coarse-grained deltas (Figures 7c and 11). More frequent channel avulsions on coarse-grained deltas result in increased periods of overbank flow. Because coarse-grained deltas are steeper than fine-grained deltas, the overbank flow on coarse-grained deltas exerts a higher shear stress on the floodplain topset. This leads to more frequent and more erosive overbank flow on coarse-grained deltas, which in turn creates more channels.

### **5.3. How Does Cohesion Control the Number of Channel Mouths?**

Previous research [*Edmonds and Slingerland, 2010*] has established a link between cohesion and number of bifurcations. *Edmonds and Slingerland* [2010] considered sediment mixtures ranging from ~55% - 96% cohesive sediment and found a peak in the number of bifurcations at intermediate cohesion. While I did not strictly measure the number of bifurcations, the number of channel mouths should be related to

the number of bifurcations provided channels are generally distributive and do not rejoin downstream from the bifurcations frequently. Indeed, the results of this study suggest that the number of channel mouths peaks at a similar value of percent cohesive sediment as that reported by *Edmonds and Slingerland* [2010], although the greatest number of channel mouths in this study are created by sediment mixtures with ~0% - 30% cohesive sediment (Figure 15b), a range in percent cohesive sediment not explored by *Edmonds and Slingerland* [2010].

The number of channel mouths in my results can be explained by considering two different process-regimes. At low median grain sizes (or high percent cohesion) the dynamics of sediment cohesion set the number of channel mouths. Distributary channels have highly stable levees that confine the flow to only a few channels and inhibit avulsions and bifurcations around river mouth bars. As the percentage of cohesive sediment is decreased to around ~70% - 80%, bifurcations around river mouth bars occur and are stabilized by the still highly cohesive levees, leading to an increase in distributary channel number. As the percent cohesive sediment is further decreased (~40% - 70%), levees and river mouth bars are unstable and easily eroded, decreasing the number of channels that form. This is consistent with the *Edmonds and Slingerland* [2010] model.

At high median grain sizes (low percent cohesion) the number of channel mouths is set by avulsion dynamics. Once the percent cohesive sediment input is below ~40%, the strong relationship between bulk cohesion and number of channel mouths breaks down (evidenced by the spread in the data in Figure 15), and the dominant process controlling the increase in number of channel mouths is channel avulsion as controlled by median grain size and topset gradient.

## 5.4. Process-Based Model for Grain Size Effects on Delta Channel Network

### Morphology and Planform Morphology

Grain size dictates delta morphology by shifting the delta into different process-regimes. I define a process-regime as a part of the model parameter space where the boundary conditions conspire to make a delta that is dominated by a given set of delta – building processes. For example, a delta dominated by a subsidence boundary condition is in an aggradation process-regime, provided sediment supply is large enough. Here I present a conceptual process-regime model for how changes in grain size modify delta-building processes and in turn, how that is expressed in the morphology. This model only considers the different process-regimes created by changes in grain size and therefore does not consider other potentially important process-regimes such as those created by crustal subsidence or wave energy.

Results from this study show that grain size of the incoming sediment load can control the topset gradient on the delta. Median grain size and cohesion set the channel network, and thus the number of channel mouths along the delta shoreline. The number of channel mouths and advection lengths of varying grain sizes set the deposition pattern along the shoreline, which translates into shoreline rugosity and delta shape patterns.

Fine-grained deltas occupy a process-regime that is dominated by levee growth. Low median grain sizes create shallow topset gradients with few distributary channels that are deep and aggrade slowly, and thus avulse infrequently (Figure 19). Fine-grained, highly cohesive sediment loads create stable levees that confine the majority of water and sediment discharge to the deep channel mouths, which promotes basinward progradation of elongate channels [Kim *et al.*, 2009; Edmonds and Slingerland, 2010; Falcini and

*Jerolmack, 2010; Rowland et al., 2010*]. These growth processes result in deltas with a few, sinuous channels, smooth shorelines, and elongate shapes.

Intermediate-grained deltas occupy a process-regime that is dominated by river mouth bar growth. Although avulsion is more frequent than in fine-grained deltas (Figure 19), channels remain in their original location long enough for river mouth bars to grow. Intermediate values of cohesion (~50% - 80% cohesive sediment) aid in stabilizing mouth bars and levees [*Edmonds and Slingerland, 2010*], leading to successful channel bifurcations at the shoreline [*Edmonds and Slingerland, 2007*] and an increase in the number of active channel mouths. The bifurcated channel network deposits sediment along the entire shoreline creating a semi-circular delta shape (Figure 13), though the increased mouth bar deposition and progradation creates local shoreline perturbations (Figures 8e and 8f), leading to the most rugose shorelines observed (Figure 12).

Coarse-grained deltas occupy a process-regime that is dominated by frequent channel avulsions. In order to maintain steeper topset gradients (Figure 17), coarse-grained deltas aggrade at faster rates than finer-grained deltas, leading to more frequent channel superelevation above the adjacent floodplain and increased avulsion frequency (Figure 19) [*Mohrig et al., 2000; Jerolmack and Mohrig, 2007*]. More frequent avulsions result in more concurrently active channels [*Makaske, 2001*] as new channels are easily eroded into the delta topset due to high shear stresses exerted on the floodplain by overbank flow. The large number of mobile channel mouths deposit sediment evenly along the delta shoreline, resulting in a semi-circular delta shape (Figure 13). The process of channel bifurcation around river mouth bars is suppressed on coarse-grained deltas, as channel mouths are highly mobile and rarely remain in one location long

enough to build a mature mouth bar. The absence of river mouth bar progradation creates smoother shorelines relative to intermediate-grained deltas (Figure 12).

The process-based model presented here provides a previously lacking mechanistic understanding of grain size effects on delta channel network and planform morphology that is in agreement with qualitative observations linking grain size to delta morphologies [McPherson *et al.*, 1987; Orton and Reading, 1993]. Changes in the grain-size distribution delivered to the delta apex shift deltas into the different process-regimes described above, resulting in variations in delta morphology related to grain size that are consistent with the previous qualitative studies. For example, it was previously shown that an increase in grain size from silt to gravel results in a morphological transition from elongate to semi-circular delta shapes [McPherson *et al.*, 1987; Orton and Reading, 1993]. Here I show that this transition is related to an increase in topset gradient and subsequent increase in avulsion frequency, creating a large number of channels on the delta topset that have a braided pattern and that deliver sediment evenly across the shoreline, creating a semi-circular shape.

### **5.5. Influence of Catchment Characteristics on Delta Morphology**

If grain size is as important as this study indicates, then a natural question is what controls the incoming grain-size distribution? To a first order, variations in natural grain-size distributions entering a delta apex result from differences in upstream catchment area characteristics. These include source properties that build the initial grain-size distribution (e.g. lithology, weathering processes), and modification of the distribution downstream by fluvial processes through abrasion and selective deposition [e.g. Ferguson *et al.*, 1996; Rice, 1999; Fedele and Paola, 2007]. The most recent effort in

quantifying this relationship is *Syvitski and Milliman's* [2007] analysis of modern sediment loads delivered to the world's coasts. They found that a majority of the between-river variation in total sediment load is a function of basin area, relief, lithology, and ice erosion. Thus, to a first order, one can relate the sediment loads delivered to a delta to its catchment characteristics. Relating sediment size to source terrain is more difficult, but in general, larger catchments with low relief deliver more predominantly fine sediment, whereas smaller catchments with high ruggedness deliver more coarse-grained sediment [*Milliman and Syvitski, 1992; Orton and Reading, 1993; Mulder and Syvitski, 1995; Syvitski and Milliman, 2007*]. Thus, my results suggest that to a first order, active margin coasts that are generally dominated by steep, high relief catchments with short transport distances should be dominated by coarse-grained deltas that are semi-circular with many active channels. Passive margin coasts with large drainage basins that drain the low-relief continental interiors and have long transport distances should deliver finer grains to the coasts and produce elongate deltas. Thus, in a sense, grain-size distribution is a function of catchment area related to a given delta. With this in mind, the model presented here may be used to connect delta morphology to catchment area, though additional work developing such predictive capabilities is necessary.

## 6. Conclusion

Natural deltas exhibit a range of morphologies not completely explained by the control of fluvial, wave, and tidal energies (Figure 1). I show that this additional, unexplained morphological variation may be attributed to variations in the grain-size distribution, primarily by the median grain size, and to a lesser extent by the standard deviation of the grain-size distribution. For example, changing median grain size alone produces delta morphologies that are qualitatively similar to natural deltas (compare deltas in Figure 1 to modeled deltas of similar median grain size in Figure 5). Analysis of 33 numerically modeled deltas shows that topset gradient and average number of channel mouths are positive functions of median grain size. Shoreline rugosity is highest at intermediate median grain sizes, and delta shapes most closely approximate a semi-circle at coarse median grain sizes. Percent cohesive sediment varies as a function of the grain-size distribution. Results reveal an overall negative relationship between percent cohesive sediment and number of channel mouths. This relationship is characterized by an additional peak in number of channel mouths around ~70% - 80% cohesive sediment that has been predicted by previous studies.

Relationships between median grain size and delta morphologies can be explained by a shift of deltas into different process-regimes, where dominant delta-building processes are expressed in the resulting delta channel network and planform morphology. To explain this control by grain size I present a process-based model for the effect of grain size on delta morphology. This model shows that (1) an increase in median grain size results in an increase in delta topset gradient, (2) as coarse-grained deltas aggrade at faster rates to maintain steeper equilibrium gradients channels avulse more frequently, (3)

increased channel avulsion leads to increased periods of overbank flow which exerts higher shear stresses on the floodplain due to steeper gradients, creating more channels on the delta topset, (4) the increased number of channel mouths delivers sediment evenly along the delta shoreline, and (5) the increased channel mobility due to increased avulsion frequency suppresses levee and river mouth bar growth at the shoreline.

Variations in median grain size from silt to coarse sand shift deltas into 3 different process-regimes, expressed as 3 end-member delta morphologies. Fine-grained deltas are dominated by levee growth and channel elongation, resulting in smooth shorelines and elongate planforms. Intermediate-grained deltas are dominated by channel bifurcations around river mouth bars, resulting in semi-circular deltas with rugose shorelines. Coarse-grained deltas are dominated by channel avulsions, resulting in semi-circular delta shapes with many channels and relatively smooth shorelines.

The grain-size distribution of the incoming sediment load is determined by upstream catchment characteristics. Thus, the relationships between grain size and resulting delta morphology presented here may aid in interpreting past catchment area characteristics related to deltaic deposition preserved in the stratigraphic record. Future work should focus on determining the degree to which the described variations in delta morphology are preserved in the stratigraphic record and test the predictive capabilities for determining past upstream catchment area characteristics. Additionally, the model for grain size effects on delta morphology presented here shows that changing grain size alone creates a large range in delta morphologies. Future work will focus on testing this model with data from natural deltaic systems, and determining the degree to which global delta morphological variation can be explained by changes in grain size.

## Notation

$a$	sediment transport relation constant, nondimensional;
$B$	channel width, m;
$\bar{B}_{cells}$	mean channel width, grid cells;
$c^i$	mass concentration of the $i$ th sediment fractions, $\text{kg m}^{-3}$ ;
$C$	Chézy value, $\text{m}^{1/2} \text{s}^{-1}$ ;
$C_{a,i}$	number of initial ‘active channel cells’ that have been ‘abandoned’ at time $i$ , grid cells;
$C_{ch,0}$	number of initial ‘active channel cells’, grid cells;
$C_{ch,i}$	number of initial ‘active channel cells’ that remain active at time $i$ , grid cells;
$D$	channel depth, m;
$\bar{D}$	average channel depth, m;
$D_{50}$	median grain size, m (unless otherwise noted);
$D_i$	grain size of the $i$ th sediment fraction, m;
$f$	Darcy-Weisbach friction factor, nondimensional;
$f_i$	weight percent of the $i$ th sediment fraction, nondimensional;
$g$	acceleration due to gravity, $\text{m s}^{-2}$ ;
$i$	time since channel initiation, yr;
$L_d$	delta length, m;
$p$	sediment transport relation constant, nondimensional;
$Q$	water discharge, $\text{m}^3 \text{s}^{-1}$ ;
$q$	water discharge per unit width, $\text{m}^2 \text{s}^{-1}$ ;
$Q_s$	suspended sediment flux, $\text{m}^3 \text{s}^{-1}$ ;
$Q_t$	total sediment flux, $\text{m}^3 \text{s}^{-1}$ ;
$q_t$	total sediment flux per unit width, $\text{m}^2 \text{s}^{-1}$ ;
$\overline{Q_t}$	time-averaged total sediment flux, $\text{m}^3 \text{s}^{-1}$ ;
$R_{ch}$	ratio of continuous channelization, nondimensional;
$s$	relative density, nondimensional;
$S$	equilibrium gradient, nondimensional;
$S_b$	magnitude of bedload transport, $\text{m}^2 \text{s}^{-1}$ ;
$Sk$	skewness of the grain-size distribution, nondimensional;
$t$	current time in delta growth, yr;
$T$	total delta growth, yr;
$T_A$	predicted channel avulsion time scale, yr;
$\overline{T_{ch}}$	measured average channel-switching time scale, yr;
$u, v, w$	depth-averaged velocity magnitudes in the $x, y,$ and $z$ directions, respectively, $\text{m s}^{-1}$ ;
$u_{cr}$	critical depth-averaged velocity; $\text{m s}^{-1}$ ;
$w_s^i$	settling velocity of the $i$ th sediment fraction, $\text{m s}^{-1}$ ;
$W_d$	delta width, m;
$X$	delta bulk shape, $W_d / 2L_d$ , nondimensional;
$\varepsilon_{s,x}^i, \varepsilon_{s,y}^i, \text{ and } \varepsilon_{s,z}^i$	eddy diffusivities in the $x, y,$ and $z$ directions, respectively, of the $i$ th sediment fraction, $\text{m}^2 \text{s}^{-1}$ ;
$\lambda$	decay rate, $\text{yr}^{-1}$ ;
$\nu$	kinematic viscosity coefficient of water, $\text{m}^2 \text{s}^{-1}$ ;

$v_A$	channel aggradation rate, $\text{m yr}^{-1}$ ;
$\rho_s$	specific density of sediment, $\text{kg m}^{-3}$ ;
$\rho_w$	specific density of water, $\text{kg m}^{-3}$ ;
$\sigma$	standard deviation of the grain-size distribution, $\phi$ ;
$\tau$	mean lifetime of an ‘active channel cell’, yr;
$\tau_0$	bed shear stress, $\text{N m}^{-2}$ ;
$\tau_{ce(C)}$	critical shear stress for erosion of cohesive sediment fractions, $\text{N m}^{-2}$ ;
$\tau_{cd(C)}$	critical shear stress for deposition of cohesive sediment fractions, $\text{N m}^{-2}$ ;
$\phi$	phi value, nondimensional;

## REFERENCES

- Ashton, A. D., and L. Giosan (2011), Wave-angle control of delta evolution, *Geophysical Research Letters*, 38(13), L13405.
- Bagnold, R. A. (1966), An approach to the sediment transport problem from general physics, *U. S. Geological Survey Professional Paper*, 37-37.
- Bhattacharya, J. P., and L. Giosan (2003), Wave-influenced deltas: geomorphological implications for facies reconstruction, *Sedimentology*, 50(1), 187-210.
- Black, K., T. Tolhurst, D. Paterson, and S. Hagerthey (2002), Working with natural cohesive sediments, *Journal of Hydraulic Engineering*, 128(1), 2-8.
- Dalrymple, R. W., and K. Choi (2007), Morphologic and facies trends through the fluvial-marine transition in tide-dominated depositional systems: a schematic framework for environmental and sequence-stratigraphic interpretation, *Earth-Science Reviews*, 81(3), 135-174.
- Dastgheib, A., J. A. Roelvink, and Z. B. Wang (2008), Long-term process-based morphological modeling of the Marsdiep Tidal Basin, *Marine Geology*, 256(1-4), 90-100.
- Deltares (2011), *Delft3D-Flow Manual 3.15.5661*, 672 pp., Delft, Netherlands.
- Edmonds, D., and R. Slingerland (2008), Stability of delta distributary networks and their bifurcations, *Water Resources Research*, 44(9), W09426.
- Edmonds, D. A., and R. L. Slingerland (2007), Mechanics of river mouth bar formation: Implications for the morphodynamics of delta distributary networks, *J Geophys Res-Earth*, 112(F2).
- Edmonds, D. A., and R. L. Slingerland (2010), Significant effect of sediment cohesion on delta morphology, *Nat Geosci*, 3(2), 105-109.
- Edmonds, D. A., R. Slingerland, J. Best, D. Parsons, and N. Smith (2010), Response of river-dominated delta channel networks to permanent changes in river discharge, *Geophysical Research Letters*, 37(12).
- Fagherazzi, S. (2008), Self-organization of tidal deltas, *Proceedings of the National Academy of Sciences of the United States of America*, 105(48), 18692-18695.
- Fagherazzi, S., and I. Overeem (2007), Models of deltaic and inner continental shelf landform evolution, *Annual Review of Earth and Planetary Sciences*, 35, 685-715.
- Falcini, F., and D. J. Jerolmack (2010), A potential vorticity theory for the formation of elongate channels in river deltas and lakes, *Journal of Geophysical Research*, 115(F4), F04038.

- Fedele, J. J., and C. Paola (2007), Similarity solutions for fluvial sediment fining by selective deposition, *Journal of Geophysical Research*, 112(F2), 0-F02038.
- Ferguson, R., T. Hoey, S. Wathen, and A. Werritty (1996), Field evidence for rapid downstream fining of river gravels through selective transport, *Geology*, 24(2), 179-182.
- Folk, R. L. (1974), *Petrology of sedimentary rocks*, Hemphill Pub. Comp., Austin, Texas, United States (USA).
- Galloway, W. E. (1975), *Process framework for describing the morphologic and stratigraphic evolution of deltaic depositional systems*, Houston Geol. Soc., Houston, Texas, United States (USA).
- Geleynse, N., J. E. A. Storms, M. J. F. Stive, H. R. A. Jagers, and D. J. R. Walstra (2010), Modeling of a mixed-load fluvio-deltaic system, *Geophysical Research Letters*, 37(05).
- Geleynse, N., J. E. A. Storms, D. J. R. Walstra, H. R. A. Jagers, Z. B. Wang, and M. J. F. Stive (2011), Controls on river delta formation; insights from numerical modelling, *Earth Planet Sc Lett*, 302(1-2), 217-226.
- Hajek, E. A., S. V. Huzurbazar, D. Mohrig, R. M. Lynds, and P. L. Heller (2010), Statistical characterization of grain-size distributions in sandy fluvial systems, *J Sediment Res*, 80(2), 184-192.
- Heller, P. L., and C. Paola (1996), Downstream changes in alluvial architecture: An exploration of controls on channel-stacking patterns, *J Sediment Res*, 66(2), 297-306.
- Hooke, R. L., and W. L. Rohrer (1979), Geometry of alluvial fans; effect of discharge and sediment size, *Earth Surface Processes*, 4(2), 147-166.
- Hoyal, D. C. J. D., and B. A. Sheets (2009), Morphodynamic evolution of experimental cohesive deltas, *Journal of Geophysical Research*, 114(F2), 0-Citation F02009.
- Hu, K., P. Ding, Z. Wang, and S. Yang (2009), A 2D/3D hydrodynamic and sediment transport model for the Yangtze Estuary, China, *Journal of Marine Systems*, 77(1), 114-136.
- Ikeda, S. (1982), Incipient motion of sand particles on side slopes, *Journal of the Hydraulics Division*, 108(HY1), 95-114.
- Jerolmack, D. J. (2009), Conceptual framework for assessing the response of delta channel networks to Holocene sea-level rise, *Quaternary Science Reviews*, 28(17-18), 1786-1800.

- Jerolmack, D. J., and J. B. Swenson (2007), Scaling relationships and evolution of distributary networks on wave-influenced deltas, *Geophysical Research Letters*, 34(23), L23402.
- Jerolmack, D. J., and D. Mohrig (2007), Conditions for branching in depositional rivers, *Geology*, 35(5), 463-466.
- Kim, W., A. Dai, T. Muto, and G. Parker (2009), Delta progradation driven by an advancing sediment source: Coupled theory and experiment describing the evolution of elongated deltas, *Water Resources Research*, 45(6), W06428.
- Lesser, G. R., J. A. Roelvink, J. A. T. M. van Kester, and G. S. Stelling (2004), Development and validation of a three-dimensional morphological model, *Coastal Engineering*, 51(8-9), 883-915.
- Makaske, B. (2001), Anastomosing rivers: a review of their classification, origin and sedimentary products, *Earth-Science Reviews*, 53(3), 149-196.
- Marciano, R., Z. B. Wang, A. Hibma, H. J. de Vriend, and A. Defina (2005), Modeling of channel patterns in short tidal basins, *Journal of Geophysical Research*, 110(F1), 13-13.
- Martin, J., B. Sheets, C. Paola, and D. Hoyal (2009), Influence of steady base-level rise on channel mobility, shoreline migration, and scaling properties of a cohesive experimental delta, *Journal of Geophysical Research*, 114(F3), 0-Citation F03017.
- McPherson, J. G., G. Shanmugam, and R. J. Moinola (1987), Fan-deltas and braid deltas; varieties of coarse-grained deltas, *Geol Soc Am Bull*, 99(3), 331-340.
- Milliman, J. D., and J. P. M. Syvitski (1992), Geomorphic/tectonic control of sediment discharge to the ocean: the importance of small mountainous rivers, *The Journal of Geology*, 525-544.
- Mohrig, D., P. L. Heller, C. Paola, and W. J. Lyons (2000), Interpreting avulsion process from ancient alluvial sequences: Guadalope-Matarranya system (northern Spain) and Wasatch Formation (western Colorado), *Geol Soc Am Bull*, 112(12), 1787-1803.
- Mulder, T., and J. P. Syvitski (1995), Turbidity currents generated at river mouths during exceptional discharges to the world oceans, *The Journal of Geology*, 285-299.
- Nardin, W., and S. Fagherazzi (2012), The effect of wind waves on the development of river mouth bars, *Geophysical Research Letters*, 39(12), L12607.
- Orton, G. J., and H. G. Reading (1993), Variability of Deltaic Processes in Terms of Sediment Supply, with Particular Emphasis on Grain-Size, *Sedimentology*, 40(3), 475-512.

- Partheniades, E. (1965), Erosion and deposition of cohesive soils, *Journal of the Hydraulics Division, ASCE*, 91(1), 105-139.
- Postma, G. (1990), Depositional architecture and facies of river and fan deltas; a synthesis, *Special Publication of the International Association of Sedimentologists*, 10, 13-27.
- Rice, S. (1999), The nature and controls on downstream fining within sedimentary links, *J Sediment Res*, 69(1), 32-39.
- Rowland, J. C., W. E. Dietrich, and M. T. Stacey (2010), Morphodynamics of subaqueous levee formation: Insights into river mouth morphologies arising from experiments, *Journal of Geophysical Research*, 115(F4), F04007.
- Shaw, J. B., M. A. Wolinsky, C. Paola, and V. R. Voller (2008), An image-based method for shoreline mapping on complex coasts, *Geophysical Research Letters*, 35(12), L12405.
- Slingerland, R., and N. D. Smith (2004), River avulsions and their deposits, *Annu. Rev. Earth Planet. Sci.*, 32, 257-285.
- Syvitski, J. P. M., and J. D. Milliman (2007), Geology, Geography, and Humans Battle for Dominance over the Delivery of Fluvial Sediment to the Coastal Ocean, *The Journal of Geology*, 115(1), 1-19.
- Syvitski, J. P. M., and Y. Saito (2007), Morphodynamics of deltas under the influence of humans, *Global and Planetary Change*, 57(3-4), 261-282.
- Taylor, J. R. (1997), *An introduction to error analysis*, 327 pp., Univ. Sci. Books, Sausalito, California, United States (USA).
- Törnqvist, T. E., and J. S. Bridge (2002), Spatial variation of overbank aggradation rate and its influence on avulsion frequency, *Sedimentology*, 49(5), 891-905.
- van Maren, D. S. (2007), Grain size and sediment concentration effects on channel patterns of silt-laden rivers, *Sedimentary Geology*, 202(1-2), 297-316.
- van Maren, D. S., J. C. Winterwerp, B. S. Wu, and J. J. Zhou (2009), Modelling hyperconcentrated flow in the Yellow River, *Earth Surface Processes and Landforms*, 34(4), 596-612.
- Van Rijn, L. C. (1993), *Principles of sediment transport in rivers, estuaries and coastal seas*, Aqua publications, Amsterdam.
- Whipple, K. X., G. Parker, C. Paola, and D. Mohrig (1998), Channel Dynamics, Sediment Transport, and the Slope of Alluvial Fans: Experimental Study, *The Journal of Geology*, 106(6), 677-694.